A post print of a published manuscript at *Computers and Geosciences*

Small baseline InSAR time series analysis: Unwrapping error correction and noise reduction

Zhang Yunjun[a,*], Heresh Fattahi[b], Falk Amelung[a]

[a] Rosenstiel School of Marine and Atmospheric Science, University of Miami, Miami, Florida, USA

[b] Jet Propulsion Laboratory, California Institute of Technology, Pasadena, California, USA

*Correspondence to Z. Yunjun, yzhang@rsmas.miami.edu

Abstract

We present a review of small baseline interferometric synthetic aperture radar (InSAR) time series analysis with a new processing workflow and software implemented in Python, named MintPy (https://github.com/insarlab/MintPy). The time series analysis is formulated as a weighted least squares inversion. The inversion is unbiased for a fully connected network of interferograms without multiple subsets, such as provided by modern SAR satellites with small orbital tube and short revisit time. In the routine workflow, we first invert the interferogram stack for the raw phase time-series, then correct for the deterministic phase components: the tropospheric delay (using global atmospheric models or the delay-elevation ratio), the topographic residual and/or phase ramp, to obtain the noise-reduced displacement time-series. Next, we estimate the average velocity excluding noisy SAR acquisitions, which are identified using an outlier detection method based on the root mean square of the residual phase. The routine workflow includes three new methods to correct or exclude phase-unwrapping errors for two-dimensional algorithms: (i) the bridging method connecting reliable regions with minimum spanning tree bridges (particularly suitable for islands), (ii) the phase closure method exploiting the conservativeness of the integer ambiguity of interferogram triplets (well suited for highly

redundant networks), and (iii) coherence-based network modification to identify and exclude interferograms with remaining coherent phase-unwrapping errors. We apply the routine workflow to the Galápagos volcanoes using Sentinel-1 and ALOS-1 data, assess the qualities of the essential steps in the workflow and compare the results with independent GPS measurements. We discuss the advantages and limitations of temporal coherence as a reliability measure, evaluate the impact of network redundancy on the precision and reliability of the InSAR measurements and its practical implication for interferometric pairs selection. A comparison with another open-source time series analysis software demonstrates the superior performance of the approach implemented in MintPy in challenging scenarios.

Keywords: InSAR; time series analysis; phase-unwrapping error; phase correction; Galápagos

1. Introduction

Time series Interferometric Synthetic Aperture Radar (InSAR) is a powerful geodetic technique to extract the temporal evolution of surface deformation from a set of repeated SAR images. Accuracy and precision of the retrieved surface displacement history are limited by the decorrelation of the SAR signal, the atmospheric delay and the phase-unwrapping error. Decorrelation is mainly caused by changes of the surface backscatter characteristics over time and by the non-ideal acquisition strategy of SAR satellites (Hanssen, 2001; Zebker and Villasenor, 1992). To overcome the limitations associated with early SAR satellites, including the relative long revisit time with non-regular acquisitions and the large orbit separation (baseline) between repeat acquisitions, two groups of InSAR time series techniques have been developed: persistent scatterer (PS) methods, which focus on the phase-stable point scatterers with applications limited to cities and man-made infrastructures (Ferretti et al., 2001; Hooper et al., 2004), and distributed scatterer (DS) methods, which relaxed the strict limit on the phase stability and included areas that are affected by decorrelation through the exploitation of the redundant network of interferograms. The DS methods are the focus of this paper.

Depending on the network of interferograms, DS methods can be divided into two categories. The first category uses the network of interferograms with small temporal and spatial baselines, known as small baseline subsets (SBAS) (Berardino et al., 2002; Schmidt and Bürgmann, 2003). These methods solve a system of linear observation equations using least squares estimation or L^1-norm minimization (Lauknes et al., 2011). In cases of a non-fully connected network, singular value decomposition or a regularization constraint (López-Quiroz et al., 2009) is applied to find physically sound solutions. These methods require phase-unwrapped interferograms. In cases of low interferometric coherence, an integer least squares estimator can be applied to the wrapped interferograms, but this estimator is computationally expensive (Samiei-Esfahany et al., 2016).

The second category uses the network consisting of all possible interferograms with full exploitation of the network redundancy (Ferretti et al., 2011; Fornaro et al., 2015; Guarnieri and Tebaldini, 2008). The solution is provided by the maximum likelihood estimator with performance close to the Cramér-Rao bound, the highest achievable precision (Guarnieri and Tebaldini, 2007), or by eigenvalue decomposition of the covariance matrix, which has been shown to be suboptimal for phase estimation (Ansari et al., 2018; Samiei-Esfahany et al., 2016). These methods swap the processing order and apply the network inversion as pre-processing steps for the estimation of optimal phases before phase unwrapping.

Despite the evident strengths of the full network approaches, especially the capability of phase estimation on low coherent areas, they remain computationally inefficient relative to the small baseline network approaches. Herein, we emphasize on the algorithmic efficiency; accordingly, we implemented a weighted least squares (WLS) estimator based on SBAS method with linear optimization. This process is known as phase linking or phase triangulation (Ansari et al., 2018; Ferretti et al., 2011) and referred hereafter as network inversion. The precision of network inversion depends on the temporal behavior of decorrelation: the small baseline network approaches provide higher precision when it is fast decorrelation, while the full network approaches provide higher precision when there is weak but long-term coherence (Ansari et al., 2017; Samiei-Esfahany et al., 2016).

To separate the tropospheric delay from displacement, both PS and DS methods traditionally rely on the spatio-temporal filtering of the phase time-series by taking into account their different frequency characteristics in time and space domain and assuming a temporal deformation model (Berardino et al., 2002; Ferretti et al., 2001), which can be unrealistic in complex natural environments such as volcanic deformation. Recent developments use global atmospheric models (GAMs), MERIS, MODIS or GPS wet delay (Jolivet et al., 2011; 2014; Li et al., 2009; Onn and Zebker, 2006; Yu et al., 2018), or empirical correlation between stratified tropospheric delay and topography (Bekaert et al., 2015; Doin et al., 2009; Lin et al., 2010) to correct interferograms before network inversion. Since the contribution of tropospheric delay is a deterministic component in InSAR phase observation, it is in principle preserved in the estimated phase time-series and therefore can be mitigated in the time-series domain after network inversion. Similar swaps of the processing sequence have been applied to phase unwrapping (Guarnieri and Tebaldini, 2008) and topographic residual correction (Fattahi and Amelung, 2013).

A disconnected network of interferograms with multiple interferogram subsets biases the time-series estimation, especially when there is no overlap in temporal or spatial baseline among interferogram subsets (Lanari et al., 2004; López-Quiroz et al., 2009). For modern SAR satellites with improved orbital control and short revisit time such as Sentinel-1, the interferograms network can be easily fully connected, simplifying the network inversion into an unbiased WLS estimation of an overdetermined system. This robust inversion allows separating phase corrections from network inversion (Pepe et al., 2011).

Here we present a new processing chain for InSAR time series analysis with phase corrections in the time-series domain, in contrast to the traditional interferogram domain. We refer the time-series domain as a series of phases indexed in time order with respect to a common reference acquisition, in contrast to the interferogram domain where the phases are indexed in acquisition pairs order. The basic idea is to split the time series analysis into two steps (Pepe et al., 2011): i) invert network of interferograms for raw phase time-series and ii) separate tropospheric delay, topographic residual, timing error and orbital error from raw phase time-series to derive the displacement time-series. We also present two new methods to correct phase-unwrapping errors in interferograms unwrapped by two-dimensional phase unwrapping algorithms.

This paper is organized as follows. We first elaborate the theoretical basis of the weighted least squares estimator and evaluate the weight functions using simulated data (section 2). The phase-unwrapping error correction methods are presented in section 3. We then describe the processing chain (section 4) and apply it to data on the Galápagos volcanoes (section 5), followed by a discussion of results (section 6) and conclusions (section 7).

2. Review of weighted least squares estimator

2.1 Theoretical basis

We consider N SAR images of the same area acquired with similar imaging geometry at times $(t_1,\ldots,t_N)$, which are used to generate M interferograms coregistered to a common SAR acquisition, corrected for earth curvature and topography and spatially phase-unwrapped, referred to in the following as a stack of unwrapped interferograms. Building on Berardino et al. (2002), we model the network inversion problem as a system of M linear observation equations with the raw phase time-series $\phi = [\phi^2, \ldots, \phi^N]^T$ as the vector of the $N - 1$ unknown parameters with reference acquisition at t_1. ϕ corresponds to the observed physical path difference or range change from the SAR antenna to a ground target between each acquisition and the reference one, inclusive of all systematic components including ground deformation, atmospheric propagation delay and geometrical interferometric phase residuals such as those caused by inaccuracy in Digital Elevation Models (DEM). For each pixel, the functional model is described as:

$$\Delta\phi = \boldsymbol{A}\phi + \Delta\phi_\varepsilon \tag{1}$$

where $\Delta\phi = [\Delta\phi^1, \ldots, \Delta\phi^M]^T$ is the interferometric phase vector with $\Delta\phi^j$ as the phase of the j_{th} interferogram, $\boldsymbol{A}$ is an $M \times (N-1)$ design matrix indicating the acquisition pairs used for interferograms generation. It consists of -1, 0 and 1 for each row with -1 for reference acquisition, 1 for secondary acquisition and 0 for the rest. An example to generate $\boldsymbol{A}$ is provided in the Supplementary Information section S2.1. $\Delta\phi_\varepsilon = [\Delta\phi_\varepsilon^1, \ldots, \Delta\phi_\varepsilon^M]^T$ is the vector of interferometric phase residual that does not fulfill the zero phase closure of interferogram triplets. It includes the decorrelation noise, phase contribution due to the change of dielectric properties of ground scatterers such as soil moisture (De Zan et al., 2014; Morrison et al., 2011), processing inconsistency such as filtering, multilooking, coregistration and interpolation errors (Agram and Simons, 2015; Hanssen, 2001), and/or phase-unwrapping errors.

A fully connected network of interferograms corresponds to a full rank design matrix $\boldsymbol{A}$. Then the estimation of ϕ can be treated as an unbiased weighted least squares inversion of an overdetermined system. The solution of equation (1) can be obtained by minimizing the L^2-norm of the residual phase vector $\Delta\phi_\varepsilon$ as:

$$\hat{\phi} = argmin \, ||\boldsymbol{W}^{1/2}(\Delta\phi - \boldsymbol{A}\phi)||_2 = (\boldsymbol{A}^T\boldsymbol{W}\boldsymbol{A})^{-1}\boldsymbol{A}^T\boldsymbol{W}\Delta\phi \tag{2}$$

where $\hat{\phi}$ is the estimated raw phase time-series and $\boldsymbol{W}$ is an $M \times M$ diagonal weight matrix, discussed in detail below. The misfit between the estimated and true raw phase time-series is given as: $\hat{\phi}_\varepsilon = \phi - \hat{\phi}$. It's propagated from $\Delta\phi_\varepsilon$ through the network of interferograms.

An alternative objective function to solve equation (1) is minimizing the L^2-norm of the residual of phase velocity of adjacent acquisitions (equation (16) in Berardino et al. (2002)). Optimizations with both objective functions give nearly identical solutions for a fully connected network. For a non-fully connected network, only the minimum-norm phase velocity gives a physically sound solution (this is used by default in the software, although both objective functions are supported).

For each pixel the quality of the inverted raw phase time-series can be assessed using the temporal coherence γ_{temp} (Pepe and Lanari, 2006):

$$\gamma_{temp} = \frac{1}{M}\left|\boldsymbol{H}^T exp[j(\Delta\phi - \boldsymbol{A}\hat{\phi})]\right| \tag{3}$$

where j is the imaginary unit, $\boldsymbol{H}$ is an $M \times 1$ all-ones column vector. A threshold for temporal coherence (0.7 by default) is used to select pixels with reliable network inversion. These pixels are referred to in the following as the reliable pixels. Some limitations of this reliability measure are discussed in section 6.4. For simplicity, in what follows we add $\hat{\phi}^1 = 0$ and refer to the vector $\hat{\phi} = [\hat{\phi}^1, \dots, \hat{\phi}^N]^T$ hereafter as the inverted raw phase time-series.

Since contributions of tropospheric delays, topographic residuals and/or phase ramps are deterministic components in InSAR phase observations, they are preserved and therefore can be mitigated in the time-series domain to obtain the displacement time-series:

$$\phi^i_{dis} = \hat{\phi}^i - \hat{\phi}^i_{tropo} - \hat{\phi}^i_{geom} - \phi^i_{resid} \tag{4}$$

where $i \in [1, \ldots N]$, $\hat{\phi}^{i}_{tropo}$ represents the estimated phase contribution due to the difference in propagation delay through the troposphere between t_i and t_1; $\hat{\phi}^{i}_{geom}$ represents the estimated geometrical range difference from radar to target caused by the non-zero spatial baseline between two orbits at t_i and t_1, including the topographic phase residual due to DEM error, phase ramp due to orbital error, and possible phase ramp in range direction due to timing error of SAR satellite; ϕ^{i}_{resid} represents the residual phase, including the residual tropospheric delay, uncorrected ionospheric delay, unmodeled non-tectonic ocean tidal loads (DiCaprio and Simons, 2008), the remaining decorrelation noise and/or phase-unwrapping errors inherited from $\Delta\phi_{\varepsilon}$.

The phase introduced by orbital errors can be modeled as a linear or quadratic ramp. It can be estimated and removed using GPS (Tong et al., 2013), making InSAR measurement dependent on GPS. Considering its stochastic behavior and insignificant contribution to the uncertainty of velocity estimation compared with the atmospheric delay for most SAR satellites with precise orbits (Fattahi and Amelung, 2014), we do not correct orbital errors.

2.2 Implicit assumptions

The presented approach has two implicit simplifications. First, we assume that the residual term $\Delta\phi_{\varepsilon}$ in the phase triangulation functional model in equation (1) is zero or strictly controlled to be negligible during the least squares estimation. The assumption might not be true due to the non-conservativeness of phases in triplets of multilooked interferograms caused by the changes in the scattering mechanisms. This non-conservativeness has been attributed to soil moisture variations between SAR acquisitions (De Zan et al., 2014), which is especially significant for L-band (De Zan and Gomba, 2018) and discussed in section 3.2 and 5.3.2.

Second, we ignored the spatial correlation of decorrelation noise between pixels. This assumption is only satisfied when the SAR system resolution equals the pixel spacing. It is not the case in urban areas with strong reflecting structures, or in filtered interferograms with reduced resolution due to the cropped bandwidth (Agram and Simons, 2015).

2.3 Choice of weight function

Four different interferogram weighting strategies are implemented in the software. The first strategy is uniform or no weighting, as used in the classic SBAS approach (Berardino et al., 2002). In this case, the weight matrix $\boldsymbol{W}$ is equal to the identity matrix and the WLS inversion simplifies into an ordinary least squares inversion. The other strategies are three different forms of coherence weighting, giving observations with high coherence (low variance) more weight than observations with low coherence (high variance).

In the second strategy, interferograms are directly weighted by their spatial coherence at each pixel (Perissin and Wang, 2012; Pepe et al., 2015). The weight matrix takes the form:

$$\boldsymbol{W} = diag\{\gamma^1, \ldots, \gamma^M\} \tag{5}$$

where γ^j is the spatial coherence of the j_{th} interferogram.

In a third strategy, interferograms are weighted by the inverse of the phase variance (Tough et al., 1995). The matrix takes the form:

$$\boldsymbol{W} = diag\{1/\sigma^2_{\Delta\phi^1},...,1/\sigma^2_{\Delta\phi^M}\} \tag{6}$$

where $\sigma^2_{\Delta\phi^j}$ is the phase variance of the j_{th} interferogram calculated through the integration of the phase probability distribution function (PDF). For distributed scatterers, the phase PDF is given by equation (S15) in the Supplementary Information section S3.2 (Tough et al., 1995) and used in the software. For persistent scatterers, the Cramér-Rao bound of variance is given directly by equation (25) from Rodriguez and Martin (1992). The difference of phase PDFs between distributed scatterers and persistent scatterers tends to vanish when a large number of looks is applied (see supp. Fig. S1a). In practice, a lookup table is generated to facilitate the conversion from spatial coherence to phase variance (see supp. Fig. S1b).

The fourth strategy for interferogram weighting is the nonparametric Fisher information matrix (FIM), which accounts for the information loss due to noise and decorrelation, defined as (Samiei-Esfahany et al., 2016; Seymour and Cumming, 1994):

$$\boldsymbol{W} = diag\{\frac{2L{\gamma^1}^2}{1-{\gamma^1}^2},...,\frac{2L{\gamma^M}^2}{1-{\gamma^M}^2}\} \tag{7}$$

where L is the number of independent looks used for the estimation of spatial coherence γ^j. Note that FIM is identical to the inverse-variance matrix for persistent scatterers.

2.4 Performance assessment of weight functions using data simulations

We evaluate the performance of the different weight functions using simulated data to address the question of the optimum choice of weighting for phase estimation (Cao et al., 2015). Note that the maximum achievable precision is bounded by phase decorrelation, indicating the inverse of phase variance is the optimum choice theoretically (Guarnieri and Tebaldini, 2007).

2.4.1 Simulation setting

We generate the stack of interferograms for a sequential interferogram network with 10 connections for each image. We use the temporal and perpendicular spatial baselines from the Sentinel-1 dataset of section 5. First, we specify an arbitrary temporal deformation model and generate the corresponding interferometric phases (Fig. 1a). Then we simulate the spatial coherence of each interferogram using a decorrelation model with exponential decay for temporal decorrelation (Fig. 1b) (Hanssen, 2001; Parizzi et al., 2009; Rocca, 2007; Zebker and Villasenor, 1992). Next, we simulate the corresponding decorrelation phase noise for a given number of looks L by generating a random number with the PDF of the interferometric phase of a distributed scatterer with the given spatial coherence and number of looks and add it to the noise-free phases (Fig. 1c, for 3×1 looks). The construction of the spatial coherence from the decorrelation model and the simulation of the decorrelation noise are described in detail in the Supplementary Information section 3. Finally, we estimate the variance of the simulated interferometric phase $\sigma^2_{\Delta\phi^j}$ using windows of 5×5 pixels and transform it to equivalent spatial coherence using $\gamma^j = 1/\sqrt{1 + 2 \cdot L \cdot \sigma^2_{\Delta\phi^j}}$ (Fig. 1d) (Agram and Simons, 2015). This coherence is used to calculate the weight for the inversion.

2.4.2 Performance assessment

To quantify the performance of the time-series estimator for the four different weight functions, we evaluate the difference between the inverted phase $\hat{\phi}^i$ and the specified, true phase ϕ^i using a root mean square error (RMSE) given as $RMSE_{sim} = \sqrt{\Sigma_{i=1}^{N}(\hat{\phi}^{i} - \phi^{i})^2/(N-1)}$, where N is the number of acquisitions ($N = 98$).

Fig. 1e shows the mean RMSE for 10,000 realizations for the four different weighting approaches as a function of the number of looks. To highlight differences, we also show the difference in mean RMSE with respect to inverse-variance weighting (Fig. 1f). The three weighted approaches outperform uniform weighting with coherence weighting performing poorer than inverse-variance weighting (as shown by a positive difference in RMSE). Compared to inverse-variance weighting, FIM weighting gives similar performance for more than 15 looks and mixed performance for fewer looks. Similar mixed and unstable performance of FIM weighting for small numbers of looks has also been observed at other simulated scenarios with both higher and lower coherences (see supp. Fig. S2). This is different from a previous study which supports the superiority of FIM over inverse-variance but considered only 25 looks (Fig. 8 of Samiei-Esfahany et al., 2016). Thus, we use the inverse of phase variance as the default weight function in the software, although all four weighting strategies are supported.

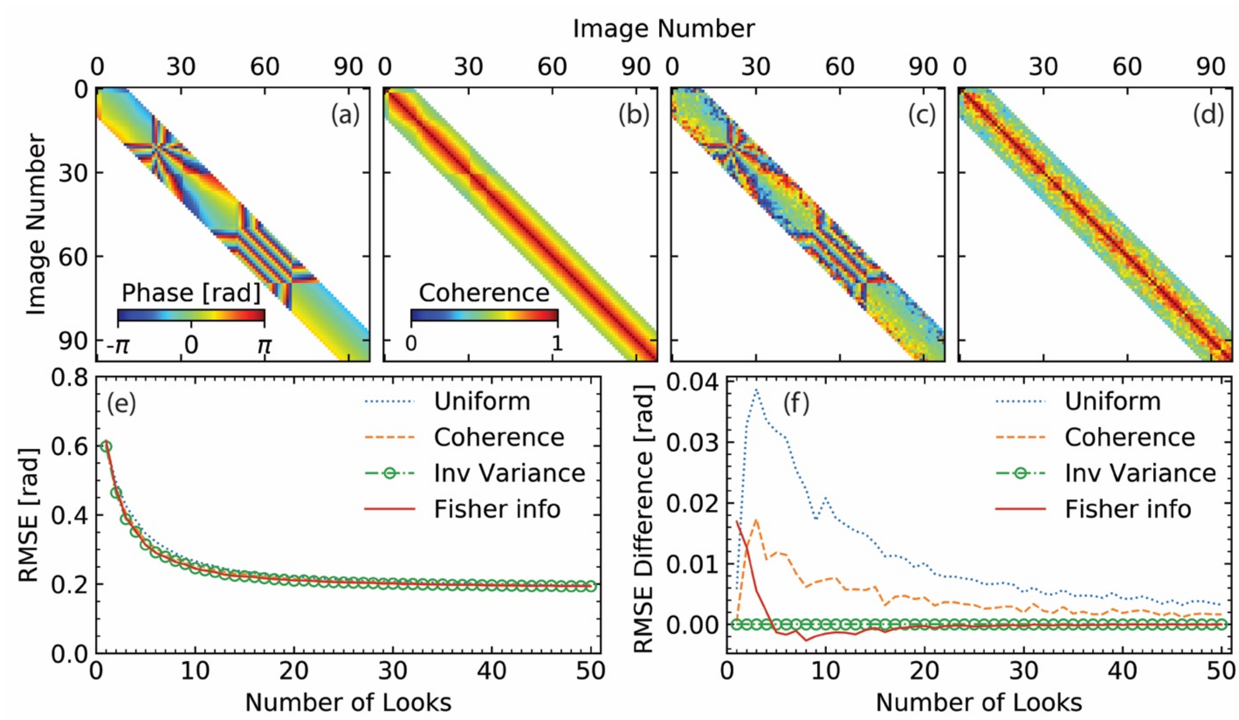

Figure 1. *Simulations for weight functions performance assessment. Upper panel: a simulated network of interferograms. (a-b) simulated (true) unwrapped phase and spatial coherence; (c) noise-containing unwrapped phase with* $L = 3 \times 1$*, (d) estimated coherence from the variance of (c). Phase data are wrapped into* $[-\pi, \pi)$ *for display. (e) Mean RMSE of 10,000 realizations of inverted phase time-series as a function of L as the performance indicator for the four weight functions. (f) Same as (e) but the difference in mean RMSE with respect to inverse-variance weighting.*

3. Unwrapping error correction

The inverted raw phase time-series can be potentially biased by wrong integer numbers of cycles (2π rad) added to the interferometric phase during the two-dimensional phase unwrapping, to which we refer simply as unwrapping errors. Here we describe two methods to automatically correct unwrapping errors using constraints from the space and time domain, respectively.

3.1 Bridging of reliable regions

In the space domain, unwrapping errors introduce phase offsets among groups of pixels that are believed to be free of relative local unwrapping errors. Such a group of pixels are referred to as a reliable region (see Chen and Zebker (2002) for a quantitative definition). These regions usually have moderate to high spatial coherence and are separated from each other due to decorrelation or high deformation phase gradients.

We assume that the phase differences between neighboring reliable regions are less than a one-half cycle (π rad) in magnitude. Then the task of unwrapping error correction is to determine the integer-cycle phase offsets to be added to each reliable region in order to align phase values among the regions. We present a bridging scheme to automatically connect reliable regions using tree searching algorithms. This is similar to region assembly in the secondary network in phase unwrapping (Carballo and Fieguth, 2002; Chen and Zebker, 2002), but in the tertiary level. To fulfill the assumption of smooth phase gradients between neighboring reliable regions, one could remove contributions from the troposphere, DEM error, deformation model, ramps before phase unwrapping and add them back in after correction. This method is particularly well suited for correcting unwrapping errors between regions separated by narrow decorrelated features such as rivers, narrow water bodies or steep topography.

3.1.1 Algorithm

The bridging scheme can be described as a three-step procedure for each interferogram. The first step is to identify reliable regions using the connected component information from the phase unwrapping algorithm such as SNAPHU (Chen and Zebker, 2001). Regions smaller than a preselected size are discarded. For each region, pixels on the boundaries are discarded using the erosion in morphological image processing with a preselected shape and size. The second step is to construct directed bridges to connect all reliable regions using the minimum spanning tree (MST) algorithm minimizing the total bridge length. We use the breadth-first algorithm to determine the order and direction (Cormen et al., 2009), starting from the largest reliable region. The third step is to estimate for each bridge the integer-cycle phase offset between the two regions. For that, we first estimate the phase difference as the difference in median values of pixels within windows of preselected size centered on the two bridge endpoints. The integer-cycle phase offset is the integer numbers of cycles to bring down the phase difference into [-π, π). The algorithm has the option to estimate a linear or quadratic phase ramp based on the largest reliable region, which is removed from the entire interferogram before the offset estimation and added back after the correction (switched off by default).

3.1.2 Simulated data

We demonstrate the bridging method using a simulated interferogram of western Kyushu, Japan (Fig. 2), a region with multiple islands, considering decorrelation noise, ground displacement, tropospheric turbulence and phase ramps. We specify spatial coherence of 0.6 and 0.001 for pixels on land and water respectively and simulate the corresponding decorrelation noise (see section 2.4.1). The simulation for the other phase contributions is shown in supp. Fig. S3. We wrap the simulated phase (Fig. 2a), unwrap using the SNAPHU algorithm, and apply the bridging method. Fig. 2b and c show the phase residual $\Delta\phi_{\varepsilon}^{i}$ after phase unwrapping (unwrapping error) without and with unwrapping error correction, respectively. The reduction in unwrapping errors (from -2π rad in orange shadings for the islands on the west in Fig. 2b to 0 rad in green shadings in Fig. 2c) demonstrates that the method works.

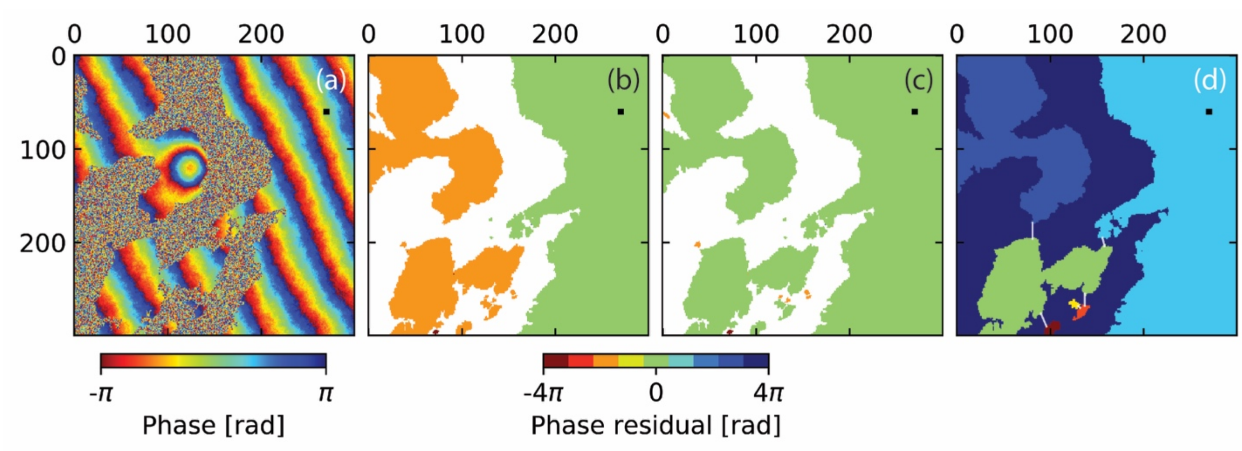

Figure 2. *Simulation of unwrapping error correction using the bridging method. (a) Simulated wrapped phase, (b and c) phase residual (unwrapping error) without and with unwrapping error correction, respectively. (d) Reliable regions and bridges (white solid lines) generated based on connected components from SNAPHU. White shadings in (b and c): areas not considered by the connected components. Black squares represent the reference point.*

3.2 Phase closure of interferogram triplets

In the time domain, unwrapping errors could break the consistency of triplets of interferometric phases (Biggs et al., 2007). The closure phase is the cyclic product of the unwrapped interferometric phases:

$$C^{ijk} = \Delta\phi^{ij} + \Delta\phi^{jk} - \Delta\phi^{ik} \tag{8}$$

where $\Delta\phi^{ij}$, $\Delta\phi^{jk}$ and $\Delta\phi^{ik}$ are three unwrapped interferometric phases generated from the SAR acquisitions at t_i, t_j and t_k. The integer ambiguity of the closure phase is given as:

$$C_{int}^{ijk} = (C^{ijk} - wrap(C^{ijk})) \,/\, (2\pi) \tag{9}$$

where *wrap* is an operator to wrap the input number into $[-\pi, \pi)$. A triplet without unwrapping errors has $C_{int}^{ijk} \equiv 0$. The number of triplets with non-zero C_{int}^{ijk} among all triplets is given as: $T_{int} = \Sigma_{i=1}^{T}(C_{int}^{i} \neq 0)$, where T is the number of triplets ($T_{int} \leq T$). T_{int} can be used to detect unwrapping errors.

Fig. 3 shows the characteristics of unwrapping errors in the closure phase from the Sentinel-1 dataset (stack of multilooked unwrapped interferograms) of section 5. The non-zero C^{ijk} in Fig. 3a and b are caused by the interferometric phase residuals (see equation (1)), whereas the non-zero C_{int}^{ijk} in Fig. 3c are caused by unwrapping errors. Fig. 3d and e show the distribution of T_{int}. On Isabela island, pixels in non-vegetated area have $T_{int} = 0$ (dark blue in Fig. 3d) and are free of unwrapping errors; while pixels in vegetated area, such as the light-blue to green area on Sierra Negra's south flank in Fig. 3d, have wide-distributed T_{int} values, indicating random unwrapping errors, which are difficult to correct. On Fernandina and Santiago island, most pixels share the common T_{int} of 229 and 576 out of 940 triplets, respectively, indicating coherent unwrapping errors and can be corrected.

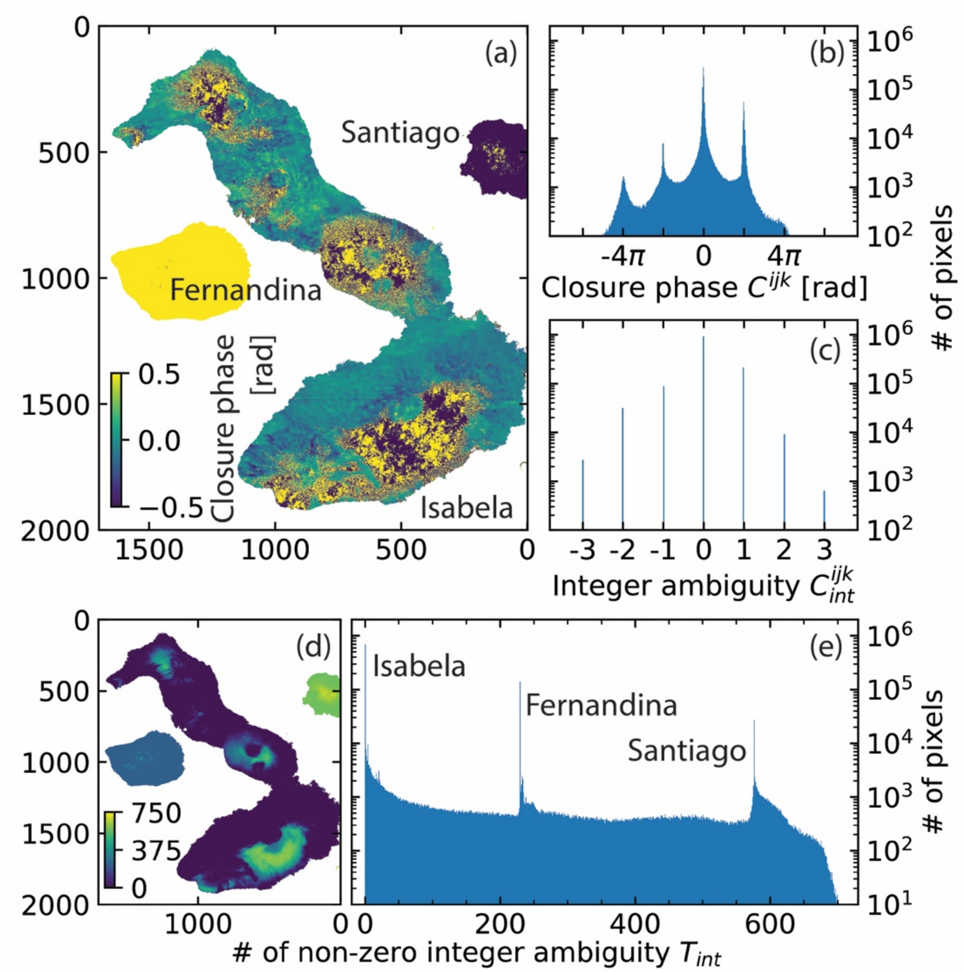

Figure 3. *Characteristics of unwrapping errors in the closure phase. (a) Map and (b) histogram of* C^{ijk} *for the interferogram triplet generated from three Sentinel-1 images acquired at 7 March 2015, 19 March 2015 and 6 May 2015 from descending track 128. (c) Histogram of* C^{ijk}_{int} *for the closure phase in (a and b). The non-zero* C^{ijk}_{int} *are caused by unwrapping errors. (d) Map and (e) histogram of* T_{int} *(the 475 interferograms from the 98 Sentinel-1 images can be combined to form 940 triplets). The spikes in (e) at 229 and 576 indicate the unwrapping error in Fernandina and Santiago island, respectively.*

Several attempts have been pursued to evaluate the phase unwrapping and correct the unwrapping errors using closure phase information. Hussain et al. (2016) use the closure phase to adjust the cost in the three-dimensional phase unwrapping procedure iteratively. Biggs et al. (2007) visually identify and correct the unwrapping errors by manually adding the integer-cycle phase offsets to badly unwrapped regions of pixels. Built on this idea, we develop an algorithm to automatically detect and correct the unwrapping errors in the network of interferograms.

3.2.1 Algorithm

For a redundant network of interferograms, the temporal consistency of the integer ambiguities of unwrapped interferometric phases can be expressed for each pixel as:

$$\boldsymbol{C}\boldsymbol{U} + (\boldsymbol{C}\Delta\varphi - wrap(\boldsymbol{C}\Delta\varphi)) \,/\, (2\pi) = 0 \tag{10}$$

where $\boldsymbol{C}$ is a $T \times M$ design matrix of all possible interferogram triplets, $\boldsymbol{U}$ is an $M \times 1$ vector of integer numbers for cycles required to meet the consistency of the interferometric phases. An example of $\boldsymbol{C}$ is provided in the Supplementary Information section S2.2. Note that equation (10) can be ill-posed and does not always has a unique solution, especially when $T < M$. Thus, regularization is required to obtain an optimal solution. We assume that the solution is more likely to be small than large, and more likely to be sparse than dense. Accordingly, we apply the L^1-norm regularized least squares optimization (Andersen et al., 2011; Xu and Sandwell, 2019), which is also known as least absolute shrinkage and selection operator (LASSO), to obtain the solution as:

$$\widehat{\boldsymbol{U}} = argmin \,||\boldsymbol{C}\boldsymbol{U} + (\boldsymbol{C}\Delta\phi - wrap(\boldsymbol{C}\Delta\phi)) \,/\, (2\pi)||_2 + \alpha||\boldsymbol{U}||_1 \tag{11}$$

where $\alpha = 0.01$ is a nonnegative parameter for the trade-off between the L^1 and L^2-norm term, with value chosen based on simulations with various values of α (see supp. Fig. S4). The corrected unwrapped interferometric phase is given as: $\Delta\phi_c = \Delta\phi + 2\pi \cdot round(\widehat{\boldsymbol{U}})$, where *round* is an operator to round the input number to the nearest integer.

3.2.2 Simulated data

We demonstrate the phase closure method using a simulated interferogram stack for one pixel (Fig. 4). We first simulate the decorrelation noise and ground deformation (see section 2.4.1) for an interferogram network with 5 sequential connections using the temporal and perpendicular spatial baselines from the Sentinel-1 dataset of section 5. Then we randomly select 20% of the interferograms to add unwrapping errors with randomly selected cycles (maximum of 2) of magnitude and randomly selected sign. Next, we apply the phase closure method and compare the unwrapping errors before and after the correction, as shown in orange and blue bars in Fig. 4a, respectively. The method decreases the number of interferograms affected by unwrapping errors from 20% to 2% and reduces the magnitude of the remaining unwrapping errors (Fig. 4a). We note that the method could potentially introduce new unwrapping errors to the unwrapped interferograms (blue bars in Fig. 4a where there is no orange bar).

We evaluate the performance of the phase closure method by comparing the input and output percentages of interferograms with unwrapping errors (before and after correction), considering different input percentages and redundancies of the interferogram network. Fig. 4b shows for 100 realizations the mean output percentage after correction versus the input percentage for networks with 3, 5 and 10 sequential interferograms. For 5 connections (orange dots in Fig. 4b), the method fully corrects unwrapping errors if there are less than 20% of interferograms affected; then the improvement slows down with the increasing input percentage until it reaches a turning point of 35%, beyond which the improvement is marginal. The maximum input percentages with full correction for 3, 5 and 10 connections are at 5, 20 and 35%, respectively, indicating better performance for more redundant networks. Fig. 4c shows the performances for 5 connections network with maximum of 2, 5 and 10 cycles of unwrapping errors. The similarity before 30% shows that the method is robust for various magnitudes of unwrapping errors. Thus, we conclude that the phase closure method is suitable for highly redundant networks of interferograms with not too many unwrapping errors.

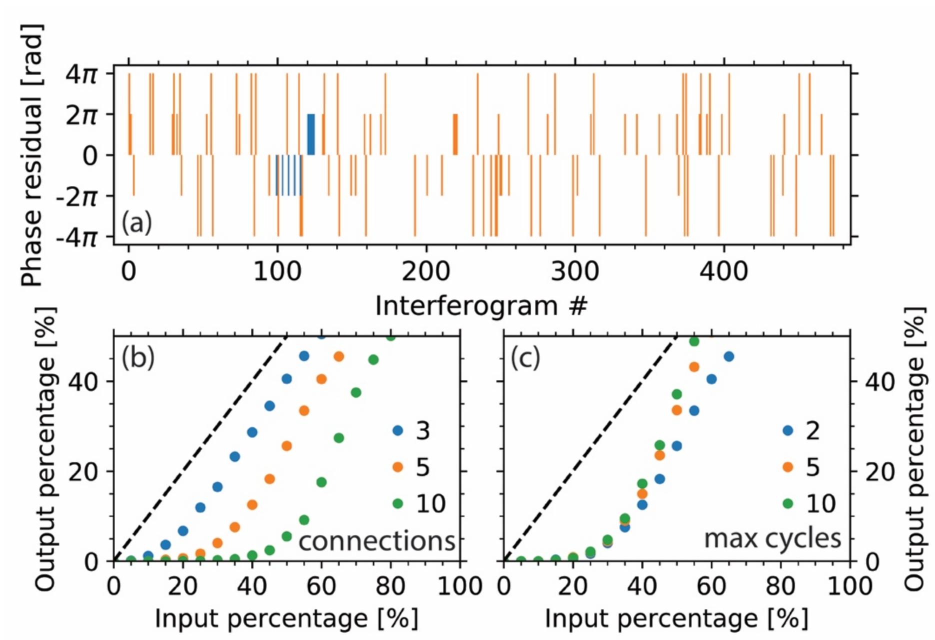

Figure 4. *Simulations of unwrapping error correction using the phase closure method. (a) Unwrapping errors in interferograms before (orange bars, account for 20%) and after correction (blue bars, account for 2%). A network of interferograms with 5 sequential connections is used. A maximum of 2 cycles of unwrapping errors are added randomly. (b) Mean output percentage of 100 realizations of interferograms with unwrapping errors versus the input*

percentage, with a fixed maximum of 2 cycles of unwrapping errors and color coded by network redundancy. (c) Same as (b) but with a fixed network of 5 connections and color coded by maximum unwrapping error magnitudes.

4. Workflow of InSAR time series analysis

We have implemented a generic routine processing workflow for InSAR time series analysis from a stack of unwrapped interferograms to displacement time-series (Fig. 5). The workflow consists of two main blocks: (i) correcting unwrapping errors and inversion for the raw phase time-series (blue ovals in Fig. 5), and (ii) correcting for phase contributions from different sources to obtain the displacement time-series (green ovals in Fig.5). It includes some optional steps, which are switched off by default (marked by dashed boundaries in Fig. 5), here we present the workflow in its most complete form. Configuration parameters for each step are initiated with default values in a customizable text file (link on GitHub).

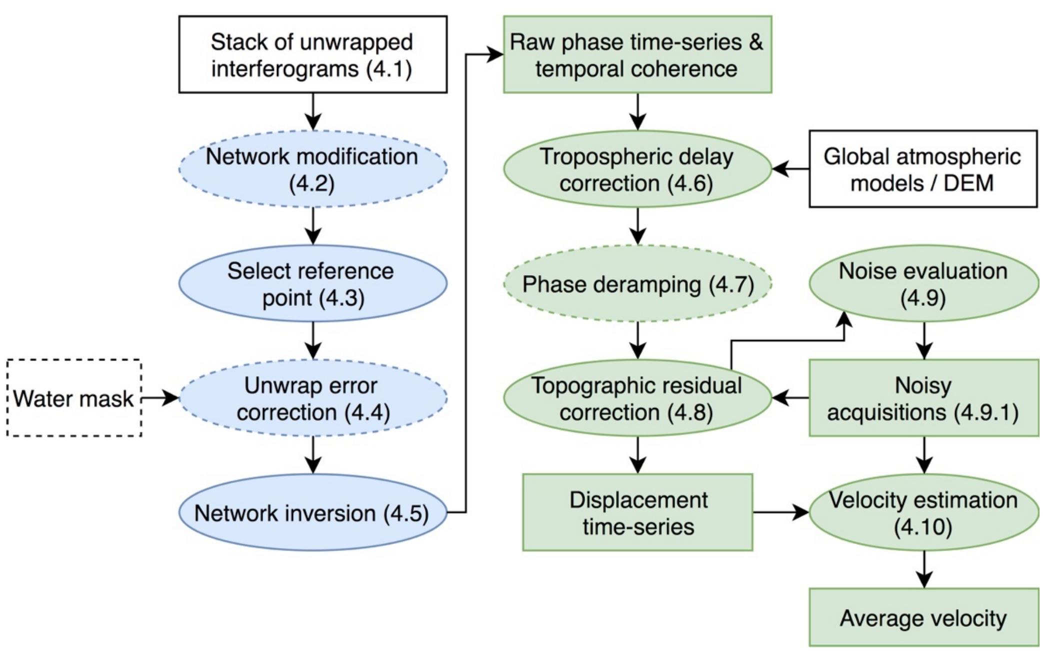

Figure 5. *Routine workflow of InSAR time series analysis. Blue ovals: steps in the interferogram domain including unwrapping error correction and network inversion; green ovals: steps in the time-series domain including phase corrections for the tropospheric delay, phase ramps, and topographic residuals. White rectangles: input data. Green rectangles: output data. Optional steps/data are marked by dashed boundaries.*

4.1 Starting point: Stack of unwrapped interferograms

As described above, the starting point is a stack of phase-unwrapped interferograms coregistered to a common SAR acquisition, corrected for earth curvature and topography. We currently support interferogram stacks produced by ISCE, GAMMA and ROI_PAC software (Rosen et al., 2004; Rosen et al, 2012; Werner et al., 2000).

4.2 Network modification

In order to exclude outliers affected by coherent pixels with unwrapping errors, the software provides network modification to exclude affected interferograms if the spatially averaged coherence for an area of interest falls below a predefined threshold value (switched off by default). This is similar to Chaussard et al. (2015) excluding interferograms with a low percentage of high coherent pixels. An extra constraint could be applied to keep those interferograms if they are part of the MST network providing the maximum spatially averaged coherence (Perissin and Wang, 2012) to ensure a fully connected network (switched on by default). The approach is referred to as coherence-based network modification. This is based on the empirical observation that reliable regions with unwrapping errors are usually surrounded by decorrelated areas. The default area of interest is all pixels on land, a customized area of interest including the decorrelated areas around the reliable regions is usually more effective. The software also supports other approaches for network modification, such as thresholds of the temporal and spatial baselines, maximum number of connections for each acquisition, and exclusion of specific acquisitions, interferograms.

4.3 Reference selection in space

The reference pixel is selected randomly among the pixels with high average spatial coherence (≥ 0.85 by default) or can be specified using prior knowledge of the study area. The reference pixel should be (i) located in a coherent area; (ii) not affected by strong atmospheric turbulence such as ionospheric streaks and (iii) close to and with similar elevation as the area of interest to minimize the impact of the spatially correlated atmospheric delay. For example, Chaussard et al. (2013) studied volcano deformation using reference points on inactive, neighboring volcanoes.

4.4 Unwrapping error correction

Three methods are available to possibly detect and correct unwrapping errors in the stack of interferograms. The first method is bridging as described in section 3.1. This method is well suited for unwrapping errors occurred among islands or on areas separated by steep topography. The second method is based on the phase closure as described in section 3.2. It's well suited for unwrapping errors in a highly redundant network of interferograms. Both methods are operated in the region level, thus are efficient. The third approach is to apply both methods, bridging followed by phase closure, as they exploit aspects of unwrapping errors in space and time domain, respectively. The default is no unwrapping error correction.

4.5 Network inversion

The raw phase time-series is solved by minimizing the interferometric phase residual $\Delta\phi_{\varepsilon}$. Then, the temporal coherence is computed based on equation (3) and used to generate a temporal coherence mask for pixels with reliable time-series estimation with a predefined threshold (0.7

by default). Pixels in shallow and water bodies are masked out if shallow mask and water body mask are available.

4.5.1 Phase masking

In order to exclude outliers affected by decorrelation, the software provides masking options (switched off by default) based on the spatial coherence (default threshold of 0.4) or using the connected component information from phase unwrapping. Note that masking based on spatial coherence is equivalent to weighting with a step function.

After masking, the pixels may have different numbers of interferograms. We use not only the pixels that are coherent in all interferograms (Agram and Simons, 2015), but relax the pixel selection criterion and also use pixels with fewer interferograms as long as a predefined minimum number of interferograms is available for each SAR acquisition (1 by default). Note that with this pixel selection strategy after masking, the network inversion result is not sensitive to the few very low coherent interferograms in a redundant network, giving robust and consistent spatial coverage.

4.6 Tropospheric delay correction

Two different approaches for tropospheric delay correction are available. In the first approach, the tropospheric delay is estimated using Global Atmospheric Models (GAMs). The estimated relative double path tropospheric delay at t_i between a given pixel p and a reference pixel is given in radians as:

$$\hat{\phi}^{i}_{tropo}(p) = \left(\delta L^{i}_{p} - \delta L^{1}_{p}\right)\frac{4\pi}{\lambda} - \left(\delta L^{i}_{ref} - \delta L^{1}_{ref}\right)\frac{4\pi}{\lambda} \quad (12)$$

where $i \in [1, \ldots N]$, δL_x^i is the integrated absolute single path tropospheric delay at t_i on pixels x in meters in satellite line-of-sight (LOS) direction (δL_p^1 for t_1) and λ is the radar wavelength in meters. The supported datasets include ERA-5 and ERA-Interim from European Center for Medium-Range Weather Forecast, NARR (North American Regional Reanalysis) from NOAA and MERRA (Modern-Era Retrospective Analysis) from NASA (applied by default, using PyAPS software from Jolivet et al. (2011; 2014)).

The second approach is based on the empirical linear relationship between the InSAR phase delay and elevation (Doin et al., 2009) which in areas with strong topographic variations sometimes outperforms corrections using GAMs. On the other hand, the empirical approach cannot distinguish between the stratified tropospheric delay and the ground deformation correlated with topography such as at volcanoes.

4.7 Phase deramping

Phase ramps are caused by residual tropospheric and ionospheric delays and to a lesser extent, by orbital errors. For long spatial wavelength deformation signals such as interseismic deformation, ramps should not be removed. Instead, physical and statistical approaches should be applied to correct the ionospheric delay (Fattahi et al., 2017; Gomba et al., 2016; Liang et al., 2018) and/or assess the measurement uncertainties (Fattahi and Amelung, 2014; 2015; Fattahi et al., 2017). For short spatial wavelength deformation signals such as volcanic deformation, landslides, and urban subsidence it is recommended to estimate and then to remove linear or quadratic ramps from the displacement time-series at each acquisition on the reliable pixels (default is no ramp removal).

4.8 Topographic residual correction

The systematic topographic phase residual caused by a DEM error is estimated based on the proportionality with the perpendicular baseline time-series (Fattahi and Amelung, 2013). The original method assumes a cubic temporal deformation model, which is not able to capture high-frequency displacement components, such as offsets caused by earthquakes or volcanic eruptions. The software provides options to account for permanent displacement jumps using step functions (Hetland et al., 2012) and to generalize polynomial functions with a user-defined polynomial order N_{poly}. The DEM error z_ε for each pixel is then given by:

$$\hat{\phi}^i - \hat{\phi}^i_{tropo} = \left(\frac{B^i_\perp}{r\sin(\theta)} z_\varepsilon + \sum_{k=0}^{N_{poly}} c_k (t_i - t_1)^k / k! + \sum_{l \in I_s} s_l H(t_i - t_l)\right) \frac{-4\pi}{\lambda} + \phi^i_{resid} \quad (13)$$

where $i \in [1, \ldots N]$, $B^i_\perp$ is the perpendicular baseline between t_i and t_1, r is the slant range between the target and the radar antenna, θ is the incidence angle, $H(t_i - t_l)$ is a Heaviside step function centered at t_l, I_s is a set of indices describing offsets at specific prior selected times. z_ε, c_k and/or s_l are the unknown parameters, which can be estimated by minimizing the L^2-norm of residual phase time-series $\phi_{resid} = [\phi^1_{resid}, \ldots, \phi^N_{resid}]^T$. An example design matrix and the numerical solution of least squares estimation are provided in the Supplementary Information section 2.3. The necessity of the step function(s) in the presence of deformation jump(s) is demonstrated in supp. Fig. S5 (default is no step function with $N_{poly} = 2$).

As we are interested in the estimation of z^ε, the assumed deformation model does not need to be a comprehensive representation of the deformation processes. Note, however, that equation (13) offers the possibility to parameterize the geophysical processes using more complex models, e.g. using the regularization functions from Hetland et al. (2012).

4.9 Residual phase for noise evaluation

The estimate of residual phase $\hat{\phi}_{resid}$, a by-product of equation (13), is the phase component that can neither be corrected nor be modeled as ground deformation, thus, is used to characterize the noise level of the InSAR time-series. For each SAR acquisition, we compute the root mean square (RMS) of the residual phase as:

$$RMS^i = \sqrt{\frac{1}{N_\Omega}\sum_{p\in\Omega}(\hat{\phi}^i_{resid}(p)\cdot\frac{\lambda}{-4\pi})^2} \tag{14}$$

where $i = [1, \ldots, N]$, $\hat{\phi}^i_{resid}(p)$ represent the residual phase at t_i for pixel p, Ω is the set of reliable pixels selected based on temporal coherence during the network inversion with the total number of N_Ω. Due to the inadequate knowledge of the long spatial wavelength phase components in $\hat{\phi}_{resid}$, we focused on the noise evaluation of the short spatial wavelength phase components only, including residual tropospheric turbulence, uncorrected ionospheric turbulence, and remaining decorrelation noise. Therefore, we remove a quadratic ramp from the residual phase of each acquisition before calculating the RMS (Lohman and Simons, 2005; Sudhaus and Jónsson, 2009).

4.9.1 Identifying noisy SAR acquisitions

Assuming the residual tropospheric delay in $\hat{\phi}_{resid}$ is stochastic and Gaussian distributed in time (Fattahi and Amelung, 2015), we can treat the noisy SAR acquisitions contaminated by severe atmospheric turbulence as outliers. Following Rousseeuw and Hubert (2011), we calculate the median absolute deviation (MAD) value and mark a SAR acquisition as noisy if its RMS value is larger than the predefined cutoff (3 MADs by default giving 99.7% confidence). Note that we assume a zero-mean value for the distribution considering the positive nature of RMS. The automatically identified noisy acquisitions will be excluded in the topographic residual estimation (during re-run) and velocity estimation.

4.9.2 Selecting the optimal reference date

The SAR acquisition with the smallest RMS value can be interpreted as the date with minimum atmospheric turbulence and is used as the reference date. We note that changing the reference date is equivalent to adding a constant to the displacement time-series, which does not change the velocity or any other information derived from the displacement time-series.

4.10 Average velocity estimation

For applications with interest on the deformation rate, the velocity v is estimated as the slope of the best fitting line to the displacement time-series, given as $\phi_{dis}^{i} \cdot \lambda/(-4\pi) = v \cdot t_i + c, i = 1, \ldots, N$, where c is an unknown offset constant. Noisy SAR acquisitions are excluded by default during the estimation. The standard deviation of the estimated velocity is given by equation (10) from Fattahi and Amelung (2015).

5. Application to Galápagos volcanoes, Ecuador

We apply the routine workflow outlined in the previous section to the western Galápagos Islands, Ecuador, located around 1000 km west of Ecuador mainland (Fig. 6 inset). We consider interferogram stacks from the Sentinel-1 and ALOS-1 satellite. For Sentinel-1 (we consider the December 2014 to June 2018 period) we use the stack Sentinel processor (Fattahi et al, 2016) within ISCE (Rosen et al, 2012) for processing the stack of interferograms; we pair each SAR image with its five nearest neighbors back in time (sequential network); we multilook each interferogram by 15 and 5 looks in range and azimuth direction respectively, filter using a Goldstein filter with a strength of 0.2 (configuration file). For ALOS-1 we use ROI_PAC (Rosen et al., 2004) for processing the stack of interferograms; we select interferometric pairs with small temporal (1800 days) and spatial baselines (1800 m) and with over 15% of Centroid doppler frequency overlap in azimuth direction; we multilook each interferogram by 8 and 16 looks in range and azimuth direction respectively, filter using a Goldstein filter with a strength of 0.5 and an adaptive smoothing with a width of 4 pixels (configuration file). We remove the topographic phase component using SRTM DEM (SRTMGL1, ~30m, 1 arc second with void-filled; Farr et al., 2007). The interferograms are phase-unwrapped using the minimum cost flow method (Chen and Zebker, 2001). In the routine workflow for the Sentinel-1 dataset we correct unwrapping errors using the bridging and phase closure method. In the routine workflow for the ALOS-1 dataset we exclude interferograms using coherence-based network modification with a customized area of interest (blue rectangle in Fig. 10b) and correct unwrapping errors using the bridging method. We remove linear phase ramps from both datasets.

The Islands host seven active volcanoes characterized by large summit calderas with several km radii and by distinguished nonlinear deformation behavior. The surface coverage ranges from bare lava flows to dense vegetation. We discuss observations of Sierra Negra, Cerro Azul, Alcedo, Wolf and Fernandina volcanoes. Sierra Negra erupted in 26 June 2018, Wolf volcano in May 2015 and Fernandina volcano in September 2017 and June 2018.

637 Products of the routine workflow include the mean LOS velocity (Fig. 6) and the displacement time-series (Fig. 7, shown for Fernandina island only). The center of Sierra Negra caldera uplifted at a mean rate of 60 cm/yr (Fig. 6) but the uplift rate varied with time (Fig. 8). The deformation at Cerro Azul volcano was caused by a sill intrusion in March 2017 (Bagnardi and Hooper, 2018).

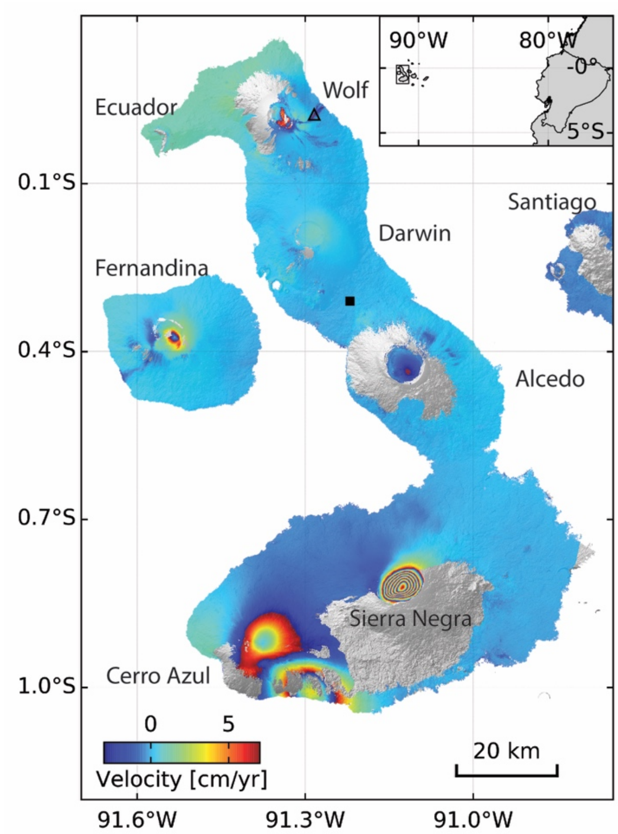

Figure 6. *Mean LOS velocity at Isabela, Fernandina, and Santiago (main image), the westernmost islands in the Galápagos archipelago (inset). The velocity is estimated from 98 Sentinel-1 descending track 128 SAR acquisitions from December 2014 to 19 June 2018 and wrapped into [-3, 7) cm/yr for display so that one color-cycle represents 10 cm/yr displacement velocity. Black square represents the reference point. Black triangle indicates the location of the pixel covered by the lava flow of the 2015 Wolf eruption used in Fig. 15b and c. Dark blue in Santiago island indicates biased velocity estimation caused by remaining unwrapping errors.*

The southeast part of the caldera of Volcán Alcedo has been subsiding at a rate of -3.1 cm/yr. The center of Fernandina caldera uplifted by 14 cm before the September 2017 eruption, subsided during the eruption and uplifted by 35 cm until the June 2018 eruption (Fig. 7).

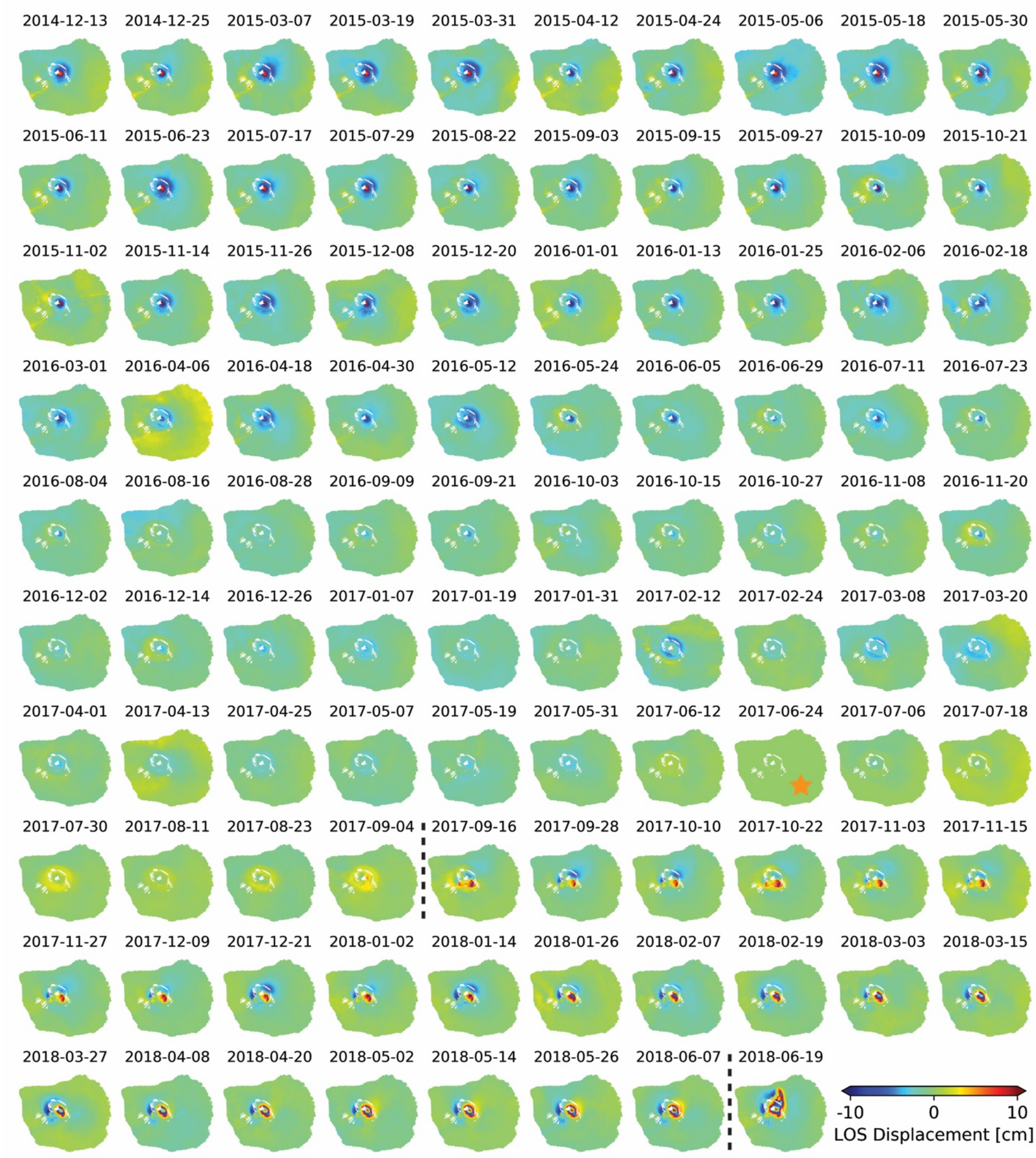

Figure 7. *Displacement time-series on Fernandina volcano with Sentinel-1 data. Dashed lines: eruption events on September 2017 and June 2018. Orange star: automatically selected reference date. The reference point is on Isabela island (black square in Fig. 6). Data are wrapped into [-10, 10) cm for display.*

5.1 Comparison with GPS

To validate the InSAR measurements we use the continuous GPS measurements at stations in the Sierra Negra caldera (circles in Fig. 8a; Blewitt et al., 2018). All three GPS components in east, north and vertical directions are used to project displacements into InSAR LOS direction. Both InSAR and GPS time-series are referenced to station GV01 in space and a common reference date in time. The InSAR data for each GPS point is obtained by linear interpolation (InSAR pixel size is $64 \times 70\ m^2$). The InSAR and GPS total displacements for the period of interest (Fig. 8a) and the displacement time-series (Fig. 8b) agree very well, except for GV10 discussed below. To quantify the agreement, we assume the GPS time-series as truth and compute the coefficient of determination R^2 between InSAR time-series and GPS time-series and the RMSE given as:

$$RMSE_{InSAR} = \sqrt{\Sigma_{i=1}^{N_{comm}} (d_{InSAR}^i - d_{GPS}^i)^2 / (N_{comm} - 1)} \qquad (15)$$

where $d_{InSAR}^i = \phi_{dis}^i \cdot \frac{\lambda}{-4\pi}$ and d_{GPS}^i are the InSAR and GPS time-series in LOS direction, respectively, at the i_{th} common date. N_{comm} is the total number of common dates.

The temporal coherence at the GPS stations varies from 0.96 to 1.0 (Fig. 8b) indicating reliable InSAR measurements at these locations (except GV10). The R^2 at the GPS stations are 1.0 and the RMSE varies from 0.5 to 1.8 cm (Fig. 8b), confirming the good agreement of the two measurements. The exception is station GV10 (R^2 of 0.72 and RMSE of 3.9 cm), which is eliminated during posterior quality assessment due to low temporal coherence of 0.64 (below the threshold of 0.7). This station is located in a more densely vegetated area outside the caldera on the rim where decorrelation due to vegetation affects the interferometric coherence (see supp. Fig. S6).

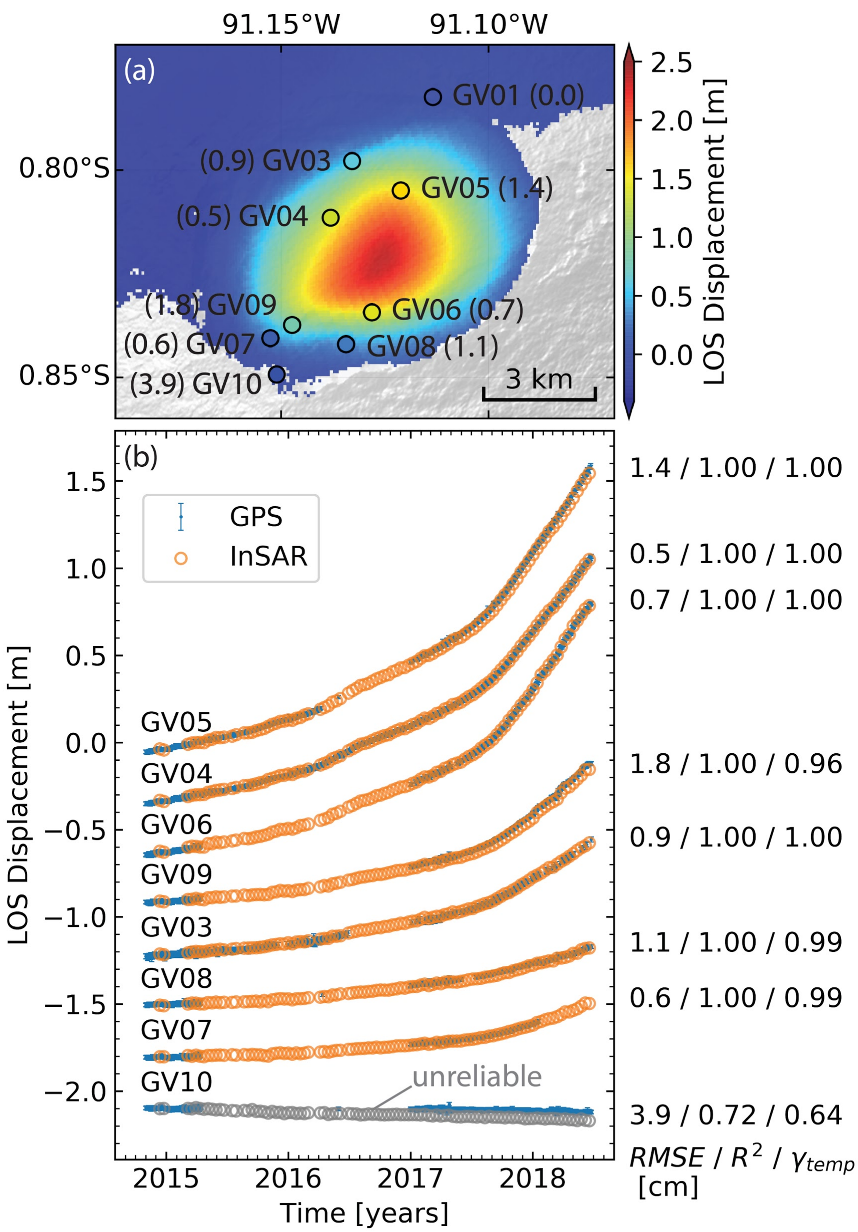

Figure 8. *Comparing InSAR with GPS. (a) Total displacements in LOS direction for Sierra Negra caldera from InSAR and GPS during 13 December 2014 - 19 June 2018. Circles: GPS stations colored by displacement. Positive displacements indicate motion towards the satellite. (b) Displacement time-series from InSAR and GPS relative to GV01 (shifted for display). Blue GPS error bars: three sigma uncertainties (in LOS direction propagated from the uncertainties in east, north and up direction). 12 April 2015 is selected as the common reference because this SAR acquisition is characterized by small residual phase RMS. Gray circles: unreliable InSAR time-series with temporal coherence less than 0.7 (masked out by default).*

5.2 Assessment of unwrapping error correction

The islands of Fernandina and Santiago exhibit unwrapping errors relative to Isabela island due to the water separation. The unwrapping errors are represented by the low temporal coherence of about 0.49 and 0.07 for Fernandina and Santiago with Sentinel-1 dataset, respectively (pixel A and B in Fig. 9a). Since there is no indication of localized submarine deformation between Isabela and Fernandina or between Isabela and Santiago during the time period of Sentinel-1 dataset, we believe the phase differences among the three islands fulfill the bridging assumption (less than π rad in magnitude). Thus, we applied the bridging method followed by the phase closure method to correct the potential unwrapping errors in the interferogram stack (Fig. 9). The bridging method leads to increased temporal coherence of 0.96 and 0.55 at these two points, respectively (Fig. 9b). The phase closure method leads to further increased temporal coherence of 1.00 and 1.00, respectively (Fig. 9c).

We note that for Santiago, however, the phase closure method did not fully correct the large amount of unwrapping errors, resulting in a biased average velocity estimation of -0.5 cm/yr

(Fig. 6). This is due to the assumption of sparse unwrapping errors in the phase closure method, which is not the case for the Sentinel-1 dataset in Santiago: 576 out of 940 interferogram triplets have non-zero integer ambiguity (Fig. 3e). Conversely temporal coherence after the phase closure correction can be partly biased.

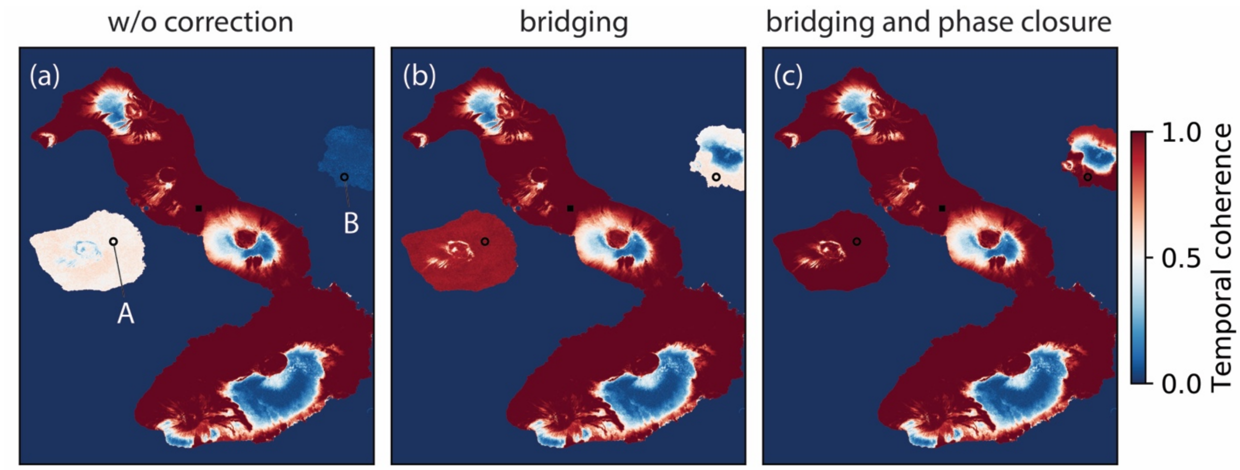

Figure 9. *Assessment of unwrapping error correction. Temporal coherence of the Sentinel-1 dataset from the network inversion of the interferogram stack (a) before the unwrapping error correction, (b) after the unwrapping error correction with bridging and (c) with bridging and phase closure. Black squares indicate the reference point.*

5.3 Assessment of network inversion

5.3.1 Temporal coherence

The quality of the network inversion can be evaluated posteriorly using the temporal coherence. In Fig. 10, we compare for the ALOS-1 dataset the temporal coherence obtained by inverting a network of small baseline interferograms using uniform weighting (classic SBAS; Fig. 10a-c) with that obtained by inverting the network after coherence-based network modification (an option of the routine workflow) using inverse-variance weighting (Fig. 10d-f). The first approach assumes an oversimplified linear relationship between the spatial coherence of each interferogram and its spatial and temporal baseline (Hooper et al., 2007; Zebker and Villasenor, 1992); while the second approach uses the observed spatial coherence on the manually specified area of interest (blue rectangle in Fig. 10b and e). This approach more reliably identifies the coherent interferograms, especially when the simple decorrelation model does not apply, e.g. vegetated areas, long temporal baseline interferograms on Sierra Negra caldera with low coherence due to high deformation phase gradient (Baran et al., 2005). The improvement in temporal coherence using the second approach leads to additional reliable pixels (Fig. 10c and f).

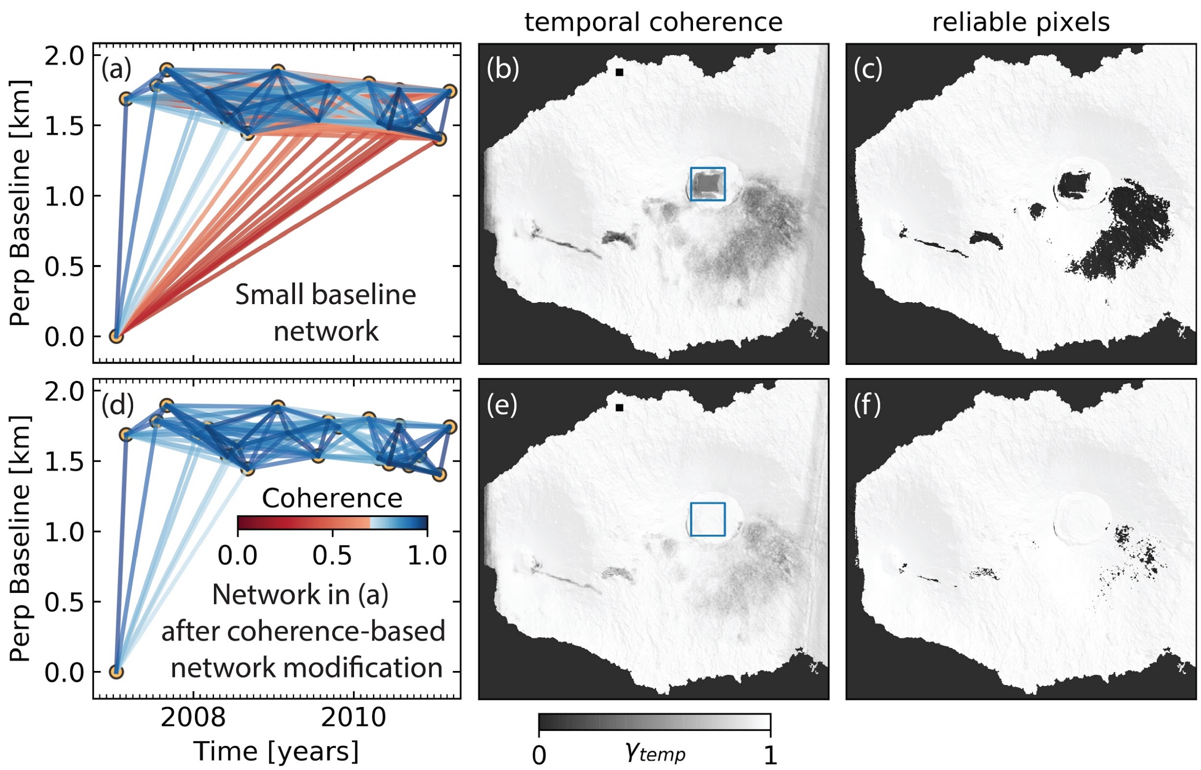

Figure 10. *Impact of network modification on temporal coherence for ALOS-1 dataset. (a) Network configuration, (b) temporal coherence and (c) reliable pixels with temporal coherence ≥ 0.7 from inversion of small baseline network with uniform weighting. (d-f): same as (a-c) but from inversion of a network obtained by coherence-based network modification with inverse-variance weighting. Lines in (a) and (d) represent interferograms colored by the average spatial*

coherence within the Sierra Negra caldera (blue rectangles in (b and e)). Black squares in (b and e) indicate the reference point.

5.3.2 Inverted raw phase

The temporal filtering performed by the inversion of a redundant network of interferograms is illustrated by comparing an observed interferogram with the interferogram reconstructed from the inverted raw phase time-series (referred to by some authors as linked phase). Fig. 11 shows an ALOS-1 interferogram with 3.5 years temporal baseline. The observed and the reconstructed interferograms (Fig. 11a and b) are very similar except at the south and east of the caldera, where the observed interferogram is incoherent but not the reconstructed interferogram as shown by the high-frequency noise in the interferogram difference (Fig. 11c). This area is forested and characterized by a low spatial coherence (Fig. 11d and e). This example, although with an extreme temporal baseline, demonstrates how the network inversion filters out the temporal decorrelation noise (Ansari, 2017; Guarnieri and Tebaldini, 2008; Pepe et al., 2015).

There is a difference in the north of the decorrelated area (yellow colors marked by white rectangle in Fig. 11c). These areas are lightly vegetated (Fig. 11e), the discrepancy in phase is likely caused by the soil or tree moisture considering its sensitivity to L-band SAR data (De Zan and Gomba, 2018) and land cover (Fig. 11e).

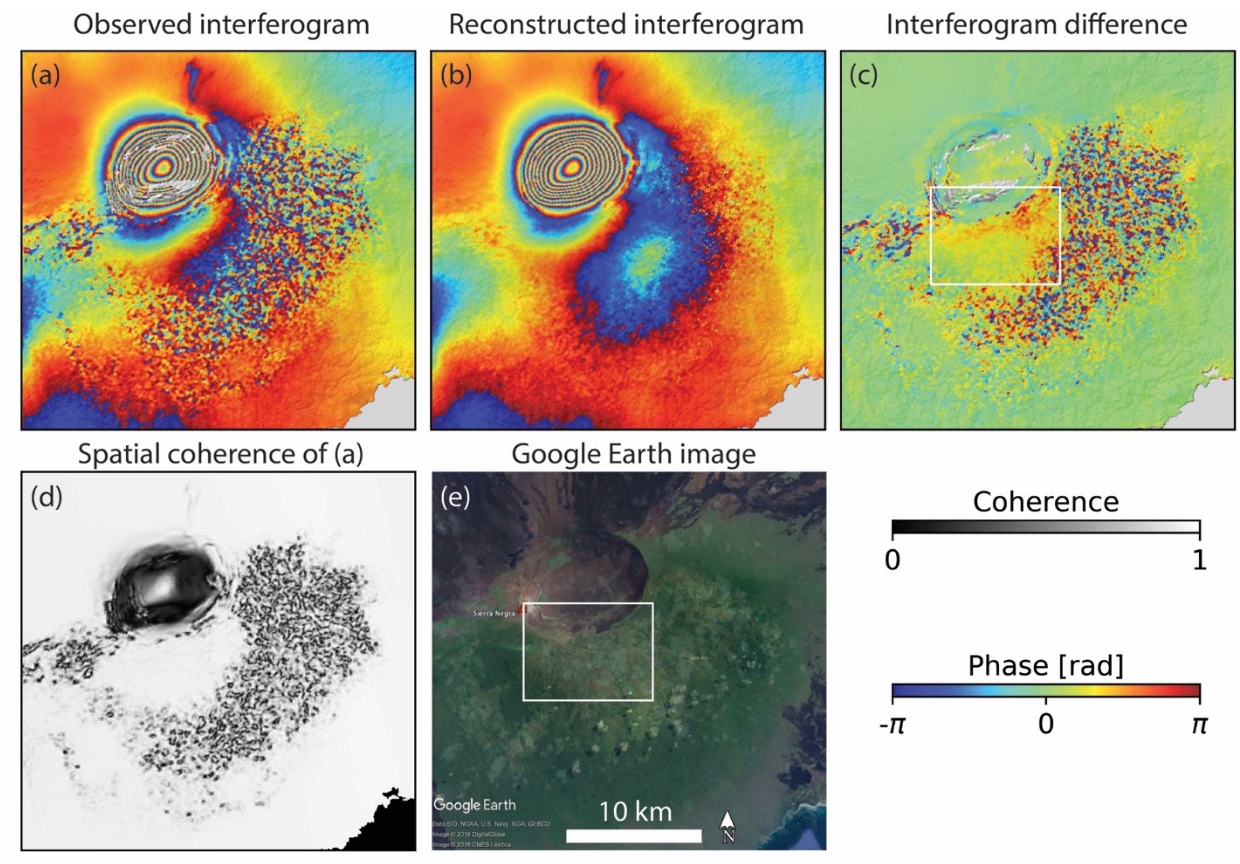

Figure 11. *Spatial inspection of the inverted raw phase. (a) Observed interferometric phase and (b) reconstructed phase from the inverted raw phase time-series; (c) difference between (a) and (b); (d) observed spatial coherence; (e) optical image from Google Earth. The ALOS-1 interferogram has temporal baseline of 3.5 years (2 March 2007 - 10 September 2010) and perpendicular baseline of 219 m. In (a) part of the caldera is masked out during phase unwrapping because of low coherence. White rectangles in (c and e): areas likely affected by soil or tree moisture. The phase is wrapped into* $[-\pi, \pi)$ *for display.*

5.4 Noisy SAR acquisitions

Noisy acquisitions with severe atmospheric delays or decorrelation noise could potentially bias the estimation of topographic residuals, the average velocity or coefficients of any temporal deformation model. In the routine workflow, they are automatically identified and excluded in the estimations.

Fig. 12 shows the impact of noisy acquisitions on the average velocity estimation for the L-band ALOS-1 dataset. Several acquisitions are severely contaminated by ionospheric streaks and identified by high residual phase RMS value (gray bars in Fig. 12a). Comparing the estimated average velocities from displacement time-series with noisy acquisitions (Fig. 12b) and without noisy acquisitions (Fig. 12c) reveals that excluding the noisy acquisitions significantly reduces the estimation bias. The residual phase time-series $\hat{\phi}_{resid}$ estimated from equation (13) is shown in supp. Fig. S7.

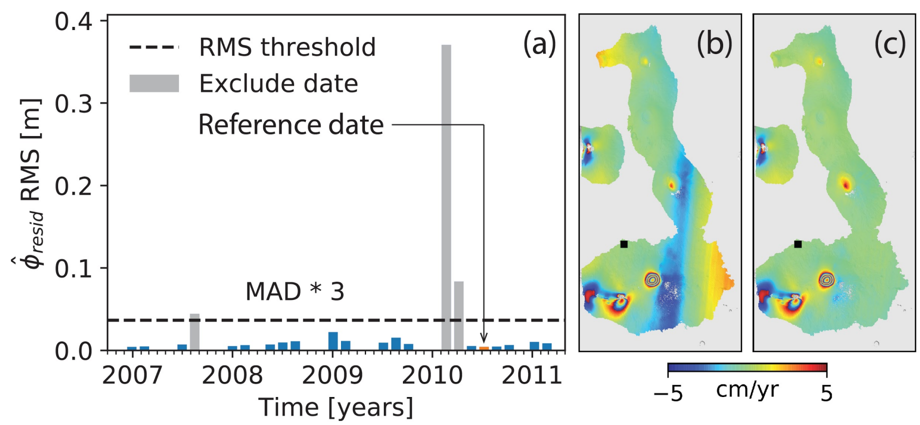

Figure 12. *Impact of noisy acquisitions on velocity estimation. (a) RMS of the residual phase estimates* $\hat{\phi}_{resid}$ *for each acquisition in the ALOS-1 dataset calculated using equation (14). Dashed line: threshold (three times MAD of the RMS time-series by default). Gray bars: noisy acquisitions with RMS larger than the threshold. (b and c): estimated average LOS velocities from displacement time-series with and without noisy acquisitions, respectively. Velocities are wrapped into [-5, 5) cm/yr for display.*

6. Discussion

6.1 Phase corrections in the time-series domain

In the presented approach the phase corrections are applied in the time-series domain in contrast to other approaches where they are applied in the interferogram domain (Agram et al., 2013; Berardino et al., 2002). Both types of approaches give identical results, but the time-series domain approach has two advantages: first, it is computationally more efficient because it uses *N-1* unwrapped phases, in contrast to the much larger number of interferograms for the interferogram domain approach (up to $N \times (N-1)/2$ for all possible interferograms); second, the impact of the corrections is readily evaluated in both the spatial and temporal domains.

Fig. 13 upper panel (a) shows how the displacement at one acquisition is obtained by subtracting the estimations of the tropospheric delay, of the phase ramp and of the topographic residual from the raw phase. The time-series for a pixel along the southern coast of Isabela demonstrates the power of the corrections (Fig. 13b). The area experienced a sill intrusion in March 2017 (dashed line in Fig. 13b; Bagnardi and Hooper, 2018). The permanent ground displacement of 5 cm in LOS direction is difficult to discern in the raw phase time-series but becomes visible after applying the three corrections. Note that this pixel is far away from the intrusion in the first stage and only affected by the intrusion in the second stage, thus showing only one jump in the displacement time-series. For Sentinel-1 the topographic residuals are small (less than 4 cm in this dataset) due to the small orbital tube but this is different for other sensors (Fattahi and Amelung, 2013).

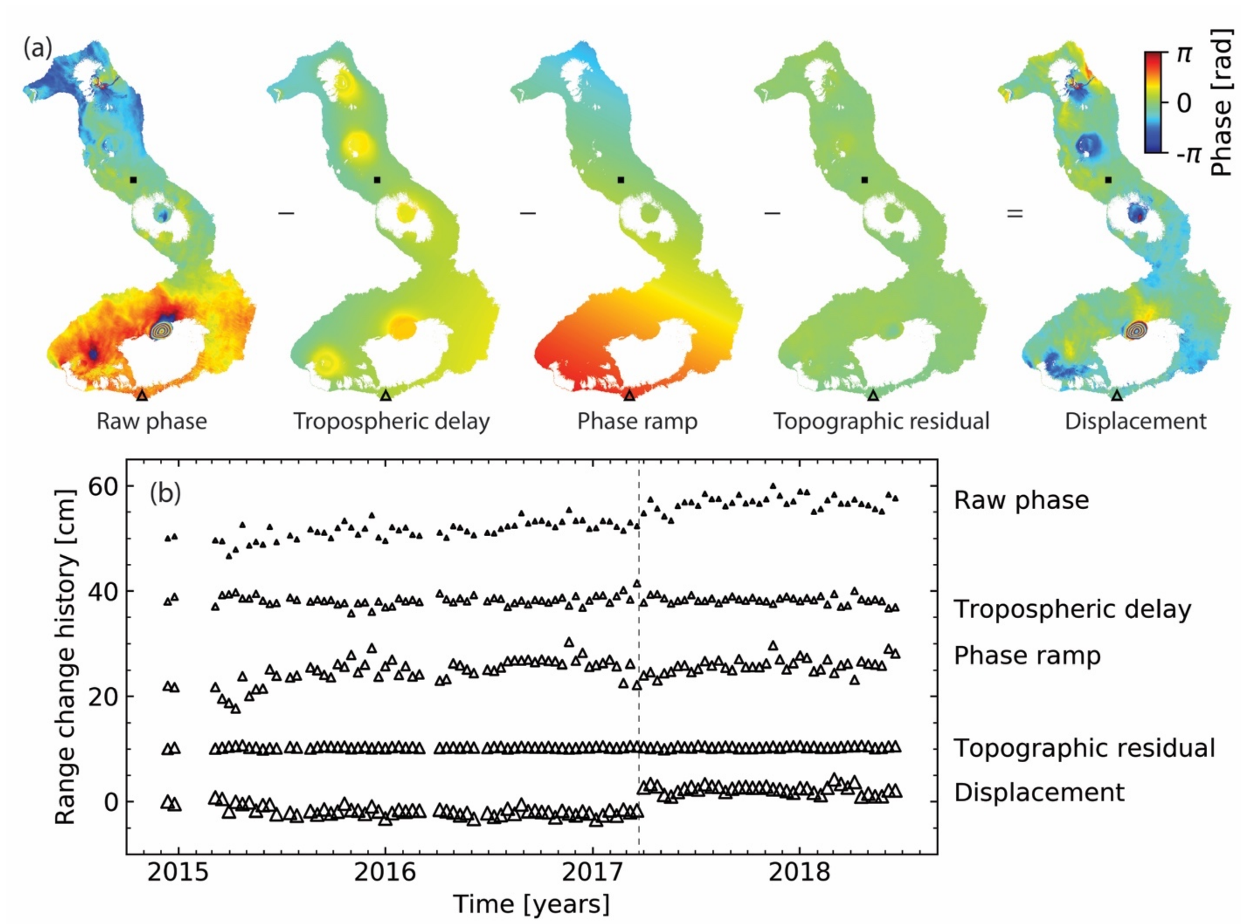

Figure 13. *Illustration of phase corrections in the time-series domain: (a) at one acquisition (12 May 2016; the reference date is 27 September 2015); (b) at one pixel (southern flank of Cerro Azul, marked as a triangle in the upper panel; [W91.1917°, S1.0352°]). Displacements are obtained by subtracting the estimated tropospheric delay, phase ramp and topographic residual from the raw phase (equation (4)). Black squares in (a) indicate the reference point. Data are wrapped into* $[-\pi, \pi)$ *for display. All range change histories in (b) start at zero but are shifted for display. The permanent displacement due to a sill intrusion in March 2017 (marked as dashed line) is visible after phase corrections.*

6.2 Order of phase corrections

In our proposed workflow the tropospheric delay correction using external independent GAMs should be applied first. The order of the other phase corrections is interchangeable because they exploit different aspects of the InSAR data. Empirical tropospheric delay correction based on delay-elevation ratio removes signals correlated with the topography. Phase deramping removes signals correlated with the spatial coordinates (linearly or quadratically). Topographic residual correction removes signals correlated in time with the perpendicular baseline. We recommend applying phase deramping before topographic residual correction so that the estimated step functions do not have to be deramped again.

6.3 Interferogram network redundancy

We consider stacks of Sentinel-1 interferograms from section 5 with different numbers of sequential connections for each acquisition to assess the impact of network redundancy on the estimation of (i) the displacement time-series and (ii) the temporal coherence (the reliability measure). We compute the RMSE of the InSAR time-series at the GPS stations within Sierra Negra caldera, assuming that the GPS measurements are the truth (see section 5.1; Fig. 14) and examine the temporal coherence for these pixels. We also count the number of reliable pixels (spatial coverage; temporal coherence ≥ 0.7).

The average RMSE (bars in Fig. 14; GV10 excluded) decreases (improves) with the increasing number of sequential connections rapidly until 5 connections then slowly until the reduction becomes negligible. The temporal coherence (orange triangles in Fig. 14) stays at high values (above 0.9) for all stations, except for GV10, for which it decreases to 0.65 at 4 connections and to 0.24 at 20 connections. The low temporal coherence indicates that this is not a reliable pixel. It also has a relatively large RMSE (Fig. 8b in section 5.1). This example shows that increasing network redundancy leads to improved identification of reliable pixels. For this specific dataset, a network of interferograms with 5 connections gives a good balance among precision, reliability and spatial coverage (green dots in Fig. 14).

We note that in this case decorrelation noise is the dominant error source. Unwrapping errors remaining after unwrapping error correction were excluded by removal of affected interferograms using coherence-based network modification (see supp. Fig. S8). Still remaining unwrap errors were suppressed by the weighting. Thus, more observations always help to reduce the stochastic decorrelation noise, resulting in a more accurate estimation of the displacement measurement (lower RMSE) and of the reliability measure (temporal coherence).

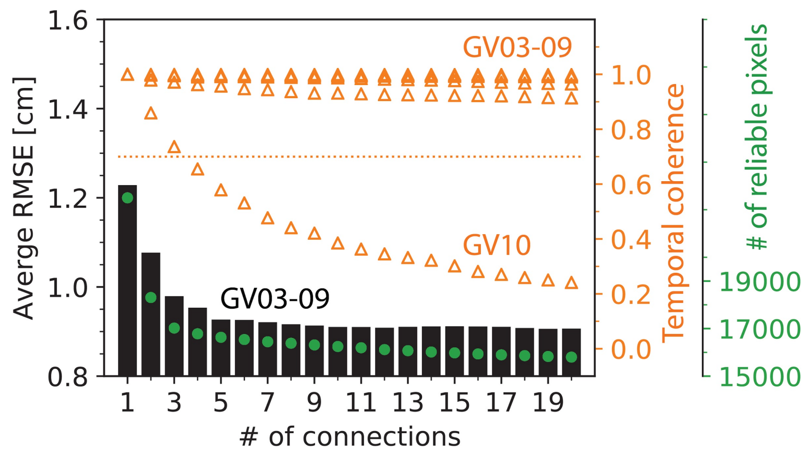

Figure 14. *Average RMSE of InSAR time-series (black bars), temporal coherence (orange triangles) at GPS stations and number of reliable pixels (green dots) as functions of the number of sequential connections. Dotted orange line: temporal coherent threshold of 0.7.*

As a practical implication, more interferograms are always preferred if the computing capacity allows (Ansari et al., 2017). Since we cannot get the estimated spatial coherence before the interferogram generation (due to the imperfect coherence model), generating a more redundant network provides room to exclude low coherent interferograms especially those containing reliable regions with unwrapping errors and still keep the network redundancy (temporal coherence would always be one and meaningless if the system of network inversion is not overdetermined, shown as orange triangles in Fig. 14 at 1 connection). In addition, a more redundant network could potentially lead to a better unwrapping error correction based on phase closure. Thus, we recommend using relatively relaxed interferogram selection thresholds (more connections in sequential networks, larger temporal and perpendicular baselines in small baseline networks) to generate more potentially coherent interferograms.

6.4 Temporal coherence as the reliability measure

We discuss the advantages and limitations of using the temporal coherence as the reliability measure. An advantage is that the temporal coherence is a more robust reliability measure for the inverted raw phase time-series compared to the average spatial coherence, because the temporal coherence indicates not only the overall decorrelation noise, but also the overall level of non-closing interferogram triplets. Non-closing triplets may be caused by the interferometric phase residual (equation (1)), including decorrelation noise, possible phase-unwrapping errors and interferometric phase contributions due to changes in the scatterers. An example of the latter is the interferometric phase caused by changes in the dielectric properties of subsurface scatterers in the result of soil moisture changes (De Zan et al., 2014; Morrison et al., 2011). Fig. 15a shows how the temporal coherence is affected by unwrapping errors. In the absence of unwrapping errors (pixels on Isabela island) the temporal and average spatial coherence are correlated but not when unwrapping errors are present (pixels on Fernandina and Santiago islands). The improvement in temporal coherence by phase-unwrapping error correction is illustrated in Fig. 9.

However, a limitation is that the temporal coherence cannot capture temporal variations of the reliability of the phase time-series. Fig. 15b and c show the displacement time-series and coherence matrix of a pixel that was covered by a lava flow during the 2015 Wolf eruption (marked as a black triangle in Fig. 6). The surface change brings down the spatial coherence to 0.3 during May-July 2015 (red grids in Fig. 15c), resulting in coherent, connected interferogram networks only before and after the lava flow emplacement. This, however, has negligible impact on the temporal coherence. With a temporal coherence of 0.94 the pixel is considered reliable although valid displacement measurements were possible only before and after the flow emplacement (after flow emplacement the pixel shows surface subsidence due to lava cooling). A three-dimensional reliability measure such as the covariance matrix of decorrelation noise (Agram and Simons, 2015) is more meaningful in this case of partially coherent scatterers, but this is beyond the scope of this manuscript.

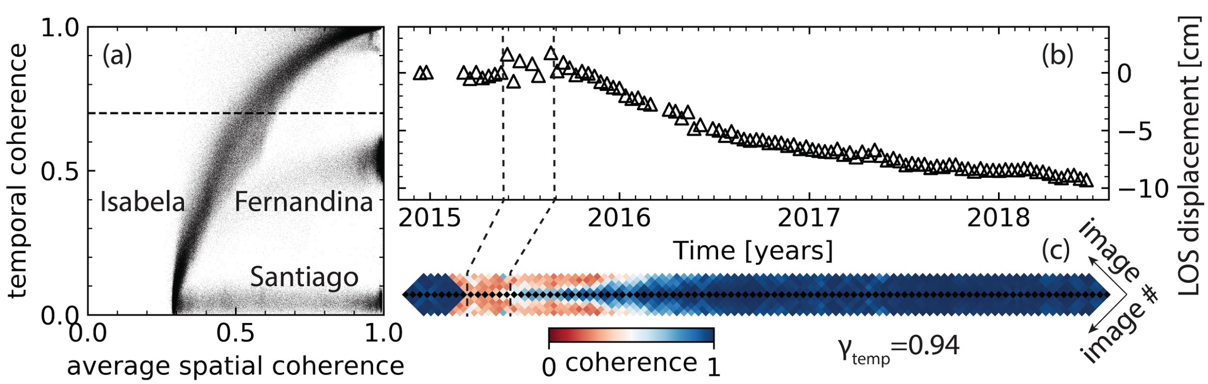

Figure 15. *Advantage and limitation of temporal coherence as reliability measure. (a) Temporal coherence versus average spatial coherence for land pixels of the Sentinel-1 dataset without unwrapping error correction. Dashed line: default temporal coherence threshold of 0.7. Three point clouds represent pixels on Isabela, Fernandina and Santiago islands. (b and c)*

Displacement time-series and the diagonal section of coherence matrix of a pixel on the lava flow of the 2015 Wolf eruption located at [W91.2838°, N0.0232°] (black triangle in Fig. 6). Reference pixel is located ~600 m to the west [W91.2891°, N0.0243°]. The coherence matrix is rotated 45° anticlockwise and shows the five diagonals below and above the main diagonal. Dashed lines: period of lava flow emplacement.

6.5 Comparing MintPy with GIAnT

We compare the performance of the MintPy routine workflow with the classic SBAS approach (Berardino et al, 2002), the New Small Baseline Subset (NSBAS) approach (Doin et al., 2011; López-Quiroz et al., 2009) and the Multiscale InSAR Time-Series approach (Hetland et al., 2012), as implemented in the Generic InSAR Analysis Toolbox (GIAnT) (Agram et al., 2013) and referred to as G-SBAS, G-NSBAS, and G-TimeFun, respectively. We use the Galápagos Sentinel-1 dataset and a spatial coherence threshold of 0.25 (as commonly done with GIAnT, Agram and Simons, 2015) for all approaches including MintPy. Tropospheric delays are corrected from the ERA-Interim model using the PyAPS software (Jolivet et al., 2011).

In the following we discuss the differences between the four approaches (summarized in table 1). We demonstrate the impact on the displacement time-series using three pixels (Fig. 16i): a high coherent pixel (pixel A), a low coherent pixel (pixel B) and a high coherent pixel with unwrapping errors and complex displacement (pixel C). The coherence matrices of the three pixels are shown in Fig. 16j. For the high coherent pixel A, all approaches give nearly identical results (Fig. 16i).

6.5.1 Initial pixel selection

MintPy selects pixels which have for every SAR acquisition a minimum number of coherent interferograms (1 by default); G-SBAS and G-TimeFun select pixels that are coherent in all interferograms; while G-NSBAS selects pixels with a predefined total minimum number of coherent interferograms (we use a minimum of 300 out of 475). This leads to differences in the spatial measurement coverage between the four approaches (Fig. 16e-h). Compared with G-SBAS and G-TimeFun, MintPy has better coverage within the calderas of Alcedo and Fernandina and along Alcedo's flank. G-NSBAS has the best spatial coverage among all approaches. The spatial coverages are shown by the distribution of the number of interferograms for pixels selected by the four approaches (Fig. 16a-d).

6.5.2 Weighted network inversion

MintPy uses weighting (the inverse-variance by default) during the network inversion while the other three approaches in GIAnT do not. The impact on the estimated displacement time-series is not negligible when there is significant quality variation among the observations. One example is the displacement time-series of the low coherent pixel B in Fig. 16i. This is confirmed by the nearly identical result between G-NSBAS and MintPy without weighting (see supp. Fig. S9a). Note that the asymmetric red grids along the horizontal black grids in Fig. 16j indicate the masked out interferogram due to spatial coherence thresholding, thus, only MintPy and G-NSBAS give estimation results.

6.5.3 Unwrapping error correction

MintPy supports bridging and phase closure methods to correct unwrapping errors in the interferograms, which GIAnT does not. Unwrap errors introduce bias in the estimated phase ramps and displacement time-series. One example is the difference of the displacement time-series on pixel C in Fig. 16i between MintPy and G-(N)SBAS. This is confirmed by the nearly identical result between G-(N)SBAS and MintPy without unwrapping error correction (see supp. Fig. S9b). The bias introduced by unwrapping errors is also evident in the velocity field at the west side of Fernandina volcano (Fig. 16e-h).

6.5.4 No deformation model

MintPy and G-SBAS do not assume temporal deformation model in network inversion. G-NSBAS and G-TimeFun require temporal deformation models: G-NSBAS uses the model only when the network is not fully connected in order to link multiple subsets of interferograms; while G-TimeFun requires over-complete, potentially redundant models, which can be added manually by user (Agram et al., 2013; Hetland et al., 2012). Thus, with the default configuration in this case, G-TimeFun did not resolve the displacement jump due to the September 2017 Fernandina eruption (pixel C in Fig. 16i).

6.5.5 Reliable pixel selection

In contrast to approaches in GIAnT, MintPy assesses the quality of the inverted phase time-series using temporal coherence and masks out unreliable pixels (gray area in Fig. 16a). We note that a higher temporal coherence threshold (0.8 instead of the default 0.7) is used because the spatial coherence thresholding reduces the number of interferograms for unreliable pixels, bringing up the temporal coherence value.

Table 1. *Summary of the differences of time series analysis approaches in MintPy and GIAnT. All approaches use small baseline network of unwrapped interferograms and linear optimization time-series estimator.*

Aspect	MintPy	G-SBAS	G-NSBAS	G-TimeFun
initial pixel selection	a minimum number of coherent interferograms for every acquisition	coherent in all interferograms	a total minimum number of coherent interferograms	coherent in all interferograms
weighted inversion	yes	no	no	no
unwrapping error correction	bridging / phase closure	no	no	no
posterior quality assessment	yes	no	no	no
prior deformation model	no	no	yes	yes
phase correction operation	time-series domain	interferogram domain	interferogram domain	interferogram domain

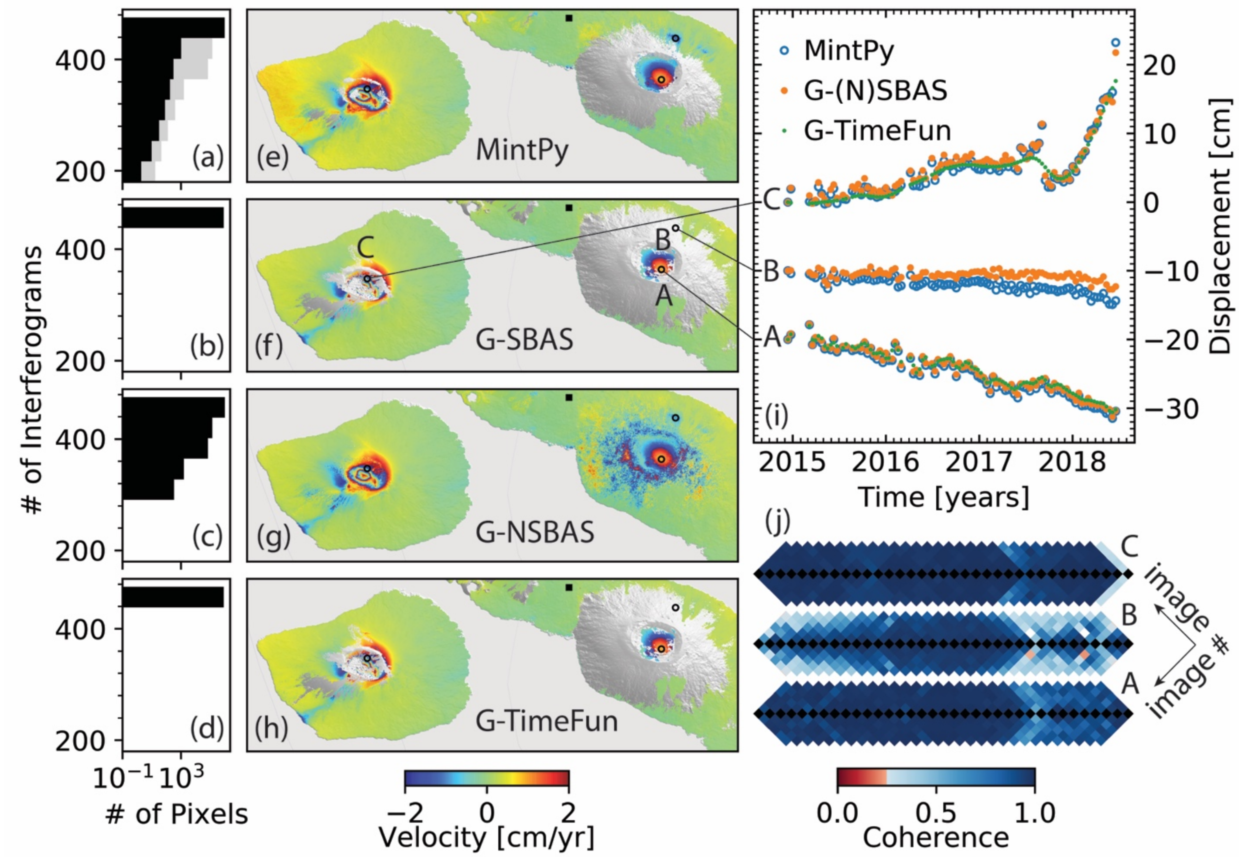

Figure 16. *Comparison of MintPy with GIAnT approaches for the Sentinel-1 dataset for the Galápagos. (a-d) Distribution of the number of interferograms for pixels used (number of pixels for each interferogram bin) by the four time-series approaches on the entire Isabela and Fernandina islands in log scale. Gray area in (a): unreliable pixels (pixels processed but discarded because of low temporal coherence). (e-h) LOS velocity estimated from the displacement time-series produced by the four time series approaches on Fernandina and Alcedo volcano. Velocities are wrapped into [-2, 2) cm/yr for display. Black squares: reference point. (i) Displacement time-series for pixels marked in (e-h). (j) Coherence matrix for pixels in (i) (rotated to make the matrix diagonal line horizontal; only showed the main diagonal and the five diagonals below and above; only showed the data from 7 May 2017 - 19 June 2018). The lower and upper half: interferograms before and after phase masking, respectively. The asymmetric*

red grids between the upper and lower half for pixel B indicate masked out interferograms with spatial coherence < 0.25.

7. Summary and conclusions

We have reviewed the mathematical formulation for the weighted network inversion and for the post-inversion phase corrections for time series analysis of small baseline InSAR stacks. In contrast to some persistent scatterer methods, the presented approach does not require prior deformation models or temporal filtering and is therefore well suited to extract nonlinear displacements. Reliable pixels are identified using the temporal coherence. Noisy acquisitions with severe atmospheric turbulence are identified using an outlier detection method based on the median absolute deviation of the residual phase RMS and are excluded during the estimations of topographic residual and average velocity.

Our workflow includes two methods to correct for, and one method to exclude remaining phase-unwrapping errors. The first unwrapping error correction method is bridging. This method uses MST bridges to connect the reliable regions of each interferogram, assuming that the phase differences between neighboring regions are less than π rad in magnitude. This method is particularly well-suited for islands and/or areas with steep topography. The second method is the phase closure method. This method exploits the conservativeness of the integer ambiguities of interferogram triplets. A sparse solution for the phase-unwrapping integer ambiguity is obtained using the L^1-norm regularized least squares approximation. Coherent phase-unwrapping errors can be identified using the distribution of the number of triplets with non-zero integer ambiguity of the closure phase. Best results are obtained by combining these two methods.

The method to exclude remaining coherent phase-unwrapping errors is coherence-based network modification. In this approach affected interferograms are identified and excluded using a threshold of average spatial coherence calculated over a customized area of interest that includes the low coherent areas surrounding the areas with coherent phase-unwrapping errors.

We have applied the routine workflow to ALOS-1 and Sentinel-1 data acquired over the Galápagos volcanoes. The InSAR results show very good agreement with independent GPS measurements. A comparison with the algorithms implemented in the GIAnT software shows similar performance in the high coherent areas but superior performance in the low coherent areas and the high coherent areas with phase-unwrapping errors or complex displacement because of unwrapping error correction, weighted network inversion, initial and reliable pixel selection using temporal coherence.

We investigated how some configurations of the routine workflow affect the precision and accuracy of the InSAR measurement using real and/or simulated data. The conclusions are:

1. Inverse-variance weighting gives the most robust and one of the best performances for network inversion among four different weighting functions: uniform, coherence, inverse-variance and Fisher information matrix.
2. For interferogram networks with 3, 5 and 10 sequential connections, the phase closure method fully corrects for phase-unwrapping errors if less than 5, 20 and 35% of the interferograms are affected by phase-unwrapping errors, respectively (with maximum

errors of 2 cycles). This shows that the phase closure method performs better for more redundant networks.

3. Increasing the network redundancy improves the network inversion and the estimation of temporal coherence (as long as phase-unwrapping errors have been corrected or excluded), resulting in more accurate estimation of the displacement time-series and identification of reliable pixels. Thus, we recommend using more connections in sequential networks, and to use larger temporal and perpendicular baselines in small baseline networks.
4. The order of the InSAR-data-dependent phase corrections (the empirical tropospheric delay correction based on the delay-elevation ratio, topographic residual correction and phase deramping) is interchangeable and has negligible impact on the noise-reduced displacement time-series.
5. Temporal coherence is a more robust reliability measure than average spatial coherence because it accounts for phase-unwrapping errors. However, it does not capture temporal variations of the reliability of the phase time-series, limiting its usefulness for partially coherent scatterers.

Author contribution

HF and ZY developed the mathematical scope. ZY and HF developed the software. ZY and FA tested the software and processed the data. ZY wrote the manuscript with the help of FA and HF. FA supervised the project.

Computer code availability

The presented workflow is implemented as the Miami INsar Time-series software in PYthon (MintPy), with open-source code, documentation, tutorials in Jupyter Notebook and test data freely available on GitHub (https://github.com/insarlab/MintPy) under GNU Generic Public License version 3. Figures in this manuscript are plotted using Jupyter Notebook and available on GitHub (https://github.com/geodesymiami/Yunjun_et_al-2019-MintPy). Time-series products from the routine workflow in this manuscript are available at https://zenodo.org/record/3464191 and displayed at https://insarmaps.miami.edu.

Declaration of competing interest

The authors declare that they have no known competing financial interests or personal relationships that could have appeared to influence the work reported in this paper.

Acknowledgments

The Sentinel-1 and ALOS-1 data were provided by ESA and JAXA, respectively, and obtained from Alaska Satellite Facility (ASF) via the Seamless SAR Archive (SSARA), a service provided by the UNAVCO facility. The ownership of ALOS-1 data belongs to JAXA and the Ministry of Economy, Trade and Industry. GPS data was provided by the University of Nevada, Reno. We thank Yunmeng Cao and Sara Mirzaee for discussions, Xiaohua Xu for pointing us to the sparse solution of the integer ambiguity of the closure phase. We thank undergraduate students Joshua Zahner, David Grossman and Alfredo Terrero for code contributions. The software is based on the initial code by Noel Gourmelen and Scott Baker. This work was supported by NASA Headquarters under the Earth and Space Science Fellowship program

(Grant No. NNX15AN13H), the NISAR Science Team (Grant No. NNX16AK52G) and National Science Foundation's Geophysics program (Grant No. EAR1345129). Part of the research was carried out at the Jet Propulsion Laboratory, California Institute of Technology, under a contract with the National Aeronautics and Space Administration.

Appendix A. Supplementary data

Supplementary data to this article can be found online at https://doi.org/10.1016/j.cageo.2019.104331.

Appendix B. List of acronyms and symbols

Table B1. List of acronyms

DS	Distributed scatterer.
FIM	Fisher information matrix.
GAM	Global atmospheric model.
GIAnT	Generic InSAR Analysis Toolbox.
G-SBAS	Small baseline subset in GIAnT.
G-NSBAS	New small baseline subset in GIAnT.
G-TimeFun	Multiscale InSAR Time-Series in GIAnT.
LASSO	Least absolute shrinkage and selection operator.
LOS	Line of sight.
MAD	Median absolute deviation.
MST	Minimum spanning tree.
PDF	Probability density function.

PS	Persistent scatterer.
RMS	Root mean square.
RMSE	Root mean square error.
SBAS	Small baseline subset.
SLC	Single look complex.
SNAPHU	Statistical-cost, Network-flow Algorithm for Phase Unwrapping.
WLS	Weighted least squares.

Table B2. List of symbols

Symbol	Parameter
$\boldsymbol{A}$	Design matrix for network inversion in size of $M \times (N-1)$.
$\boldsymbol{C}$	Design matrix for the closure phase of interferogram triplets.
$\boldsymbol{H}$	All-one column matrix in size of $M \times 1$.
L	Number of looks in range and azimuth directions in total.
M	Number of interferograms.
N	Number of SAR acquisitions.
T	Number of interferogram triplets.
$\boldsymbol{U}$	Matrix of the phase-unwrapping integer ambiguity in size of $M \times 1$.
$\boldsymbol{W}$	Weight matrix for network inversion in size of $M \times M$.
C^{ijk}	Closure phase of the interferogram triplet formed from acquisitions at t_i, t_j, and t_k.
C^{ijk}_{int}	Integer ambiguity of C^{ijk}.
T_{int}	Number of triplets with non-zero C^{ijk}_{int} among all triplets.
$\Delta\phi^j$	Interferometric phase of the j_{th} unwrapped interferogram.

$\Delta\phi_{\varepsilon}^{j}$	Interferometric phase residual of the j_{th} unwrapped interferogram.
$\Delta\phi$	Vector of the interferometric phase of all interferograms.
$\Delta\phi_{\varepsilon}$	Vector of the interferometric phase residual of all interferograms.
ϕ^{i}	Raw phase between the i_{th} and the 1_{st} acquisition.
ϕ	Vector of raw phase of all acquisitions (raw phase time-series).
$\hat{\phi}$	The estimated vector of raw phase time-series.
ϕ_{dis}^{i}	Phase due to the displacement between the i_{th} and the 1_{st} acquisition.
$\hat{\phi}_{tropo}^{i}$	Estimated tropospheric delay between the i_{th} and the 1_{st} acquisition.
$\hat{\phi}_{geom}^{i}$	Estimated geometrical range difference between the i_{th} and the 1_{st} acquisition caused by the non-zero spatial baseline.
ϕ_{resid}^{i}	Residual phase remained between the i_{th} and the 1_{st} acquisition.
ϕ_{resid}	Vector of the residual phase of all acquisitions (residual phase time-series)
$\hat{\phi}_{resid}(p)$	Estimated vector of the residual phase time-series on pixel p.
δL_{p}^{i}	Integrated absolute single path tropospheric delay between the i_{th} and the 1_{st} acquisition on pixel p in meters.
$\hat{\phi}_{tropo}^{i}(p)$	Estimated phase of the relative double path tropospheric delay between the i_{th} and the 1_{st} acquisition on pixel p with respect to pixel *ref*.
$\sigma_{\Delta\phi^{j}}^{2}$	Variance of the interferometric phase of the j_{th} interferogram.
γ^{j}	Spatial coherence of j_{th} interferogram.
γ_{temp}	Temporal coherence.
λ	Radar wavelength in meters.
z_{ε}	Topographic residual in meters.

Reference

Agram, P. S., R. Jolivet, B. Riel, Y. N. Lin, M. Simons, E. Hetland, M. P. Doin, and C. Lasserre, 2013. New Radar Interferometric Time Series Analysis Toolbox Released, *Eos, Transactions American Geophysical Union*, 94(7), 69-70, doi :10.1002/2013EO070001.

Agram, P., and M. Simons, 2015. A noise model for InSAR time series, *Journal of Geophysical Research: Solid Earth, 120*(4), 2752-2771, doi:10.1002/2014JB011271.

Andersen, M., J. Dahl, Z. Liu, and L. Vandenberghe, 2011. Interior-point methods for large-scale cone programming, in *Optimization for machine learning*, edited by S. Sra, S. Nowozin and S. J. Wright, MIT Press.

Ansari, H., F. D. Zan, and R. Bamler, 2017. Sequential Estimator: Toward Efficient InSAR Time Series Analysis, *IEEE Transactions on Geoscience and Remote Sensing, 55*(10), 5637-5652, doi:10.1109/TGRS.2017.2711037.

Ansari, H., F. D. Zan, and R. Bamler, 2018. Efficient Phase Estimation for Interferogram Stacks, *IEEE Transactions on Geoscience and Remote Sensing*, *56*(7), 4109-4125, doi:10.1109/TGRS.2018.2826045.

Bagnardi, M., and A. Hooper, 2018. Inversion of Surface Deformation Data for Rapid Estimates of Source Parameters and Uncertainties: A Bayesian Approach, *Geochemistry, Geophysics, Geosystems*, 19, doi:10.1029/2018GC007585.

Baran, I., M. Stewart, and S. Claessens, 2005. A new functional model for determining minimum and maximum detectable deformation gradient resolved by satellite radar interferometry, *IEEE Transactions on Geoscience and Remote Sensing*, *43*(4), 675-682, doi:10.1109/TGRS.2004.843187.

Bekaert, D. P. S., A. Hooper, and T. J. Wright, 2015. A spatially-variable power-law tropospheric correction technique for InSAR data, *Journal of Geophysical Research: Solid Earth, 120*(2), 1345-1356, doi:10.1002/2014JB011558.

Berardino, P., G. Fornaro, R. Lanari, and E. Sansosti, 2002. A new algorithm for surface deformation monitoring based on small baseline differential SAR interferograms, *Geoscience and Remote Sensing, IEEE Transactions on*, *40*(11), 2375-2383, doi:10.1109/TGRS.2002.803792.

Biggs, J., T. Wright, Z. Lu, and B. Parsons, 2007. Multi-interferogram method for measuring interseismic deformation: Denali Fault, Alaska, *Geophysical Journal International, 170*(3), 1165-1179, doi:10.1111/j.1365-246X.2007.03415.x.

Blewitt, G., W.C. Hammond, C. Kreemer, 2018. Harnessing the GPS Data Explosion for Interdisciplinary Science, *Eos*, 99, doi:10.1029/2018EO104623.

Cao, N., H. Lee, and H. C. Jung, 2015. Mathematical Framework for Phase-Triangulation Algorithms in Distributed-Scatterer Interferometry, *IEEE Geoscience and Remote Sensing Letters*, *12*(9), 1838-1842, doi:10.1109/LGRS.2015.2430752.

Carballo, G. F., and P. W. Fieguth, 2002. Hierarchical network flow phase unwrapping, *IEEE Transactions on Geoscience and Remote Sensing*, *40*(8), 1695-1708, doi:10.1109/TGRS.2002.800279.

Chaussard, E., F. Amelung, and Y. Aoki, 2013. Characterization of open and closed volcanic systems in Indonesia and Mexico using InSAR time series, *Journal of Geophysical Research: Solid Earth, 118*(8), 3957-3969, doi:10.1002/jgrb.50288.

Chaussard, E., R. Bürgmann, H. Fattahi, R. M. Nadeau, T. Taira, C. W. Johnson, and I. Johanson, 2015. Potential for larger earthquakes in the East San Francisco Bay Area due to the direct connection between the Hayward and Calaveras Faults, *Geophysical Research Letters, 42*(8), 2734-2741, doi:10.1002/2015GL063575.

Chen, C. W., and H. A. Zebker, 2001. Two-dimensional phase unwrapping with use of statistical models for cost functions in nonlinear optimization, *JOSA A, 18*(2), 338-351, doi:10.1364/JOSAA.18.000338.

Chen, C. W., and H. A. Zebker, 2002. Phase unwrapping for large SAR interferograms: statistical segmentation and generalized network models, *Geoscience and Remote Sensing, IEEE Transactions on*, *40*(8), 1709-1719, doi:10.1109/TGRS.2002.802453.

Cormen, T. H., C. E. Leiserson, R. L. Rivest, and C. Stein, 2009. *Introduction to algorithms*, MIT press. Chap. 22.2

De Zan, F., A. Parizzi, P. Prats-Iraola, and P. López-Dekker, 2014. A SAR Interferometric Model for Soil Moisture, *IEEE Transactions on Geoscience and Remote Sensing*, *52*(1), 418-425, doi:10.1109/TGRS.2013.2241069.

De Zan, F., and G. Gomba, 2018. Vegetation and soil moisture inversion from SAR closure phases: First experiments and results, *Remote Sensing of Environment*, *217*, 562-572, doi:10.1016/j.rse.2018.08.034.

DiCaprio, C. J., and M. Simons, 2008. Importance of ocean tidal load corrections for differential InSAR, *Geophysical Research Letters, 35*(22), doi:10.1029/2008GL035806.

Doin, M. P., C. Lasserre, G. Peltzer, O. Cavalié, and C. Doubre, 2009. Corrections of stratified tropospheric delays in SAR interferometry: Validation with global atmospheric models, *Journal of Applied Geophysics*, *69*(1), 35-50, doi:10.1016/j.jappgeo.2009.03.010.

Doin, M.-P., Lodge, F., Guillaso, S., Jolivet, R., Lasserre, C., Ducret, G., Grandin, R., Pathier, E., Pinel, V., 2011. In: Presentation of the small baseline NSBAS processing chain on a case example: the Etna deformation monitoring from 2003 to 2010 using Envisat data. Proceedings of the Fringe Symposium (SP-697), pp. 1–7.

Farr, T. G., et al., 2007. The Shuttle Radar Topography Mission, *Reviews of Geophysics*, 45(2), doi:10.1029/2005RG000183.

Fattahi, H., and F. Amelung, 2013. DEM Error Correction in InSAR Time Series, *Geoscience and Remote Sensing, IEEE Transactions on*, *51*(7), 4249-4259, doi:10.1109/TGRS.2012.2227761.

Fattahi, H., and F. Amelung, 2014. InSAR uncertainty due to orbital errors, *Geophysical Journal International*, 199(1), 549-560, doi:10.1093/gji/ggu276.

Fattahi, H., and F. Amelung, 2015. InSAR bias and uncertainty due to the systematic and stochastic tropospheric delay, *Journal of Geophysical Research: Solid Earth, 120*(12), 8758-8773, doi:10.1002/2015JB012419.

Fattahi, H., P. Agram, and M. Simons, 2016. A Network-Based Enhanced Spectral Diversity Approach for TOPS Time-Series Analysis, *IEEE Transactions on Geoscience and Remote Sensing*, *55*(2), 777-786, doi:10.1109/TGRS.2016.2614925.

Fattahi, H., M. Simons, and P. Agram, 2017. InSAR Time-Series Estimation of the Ionospheric Phase Delay: An Extension of the Split Range-Spectrum Technique, *IEEE Transactions on Geoscience and Remote Sensing*, *55*(10), 5984-5996, doi:10.1109/TGRS.2017.2718566.

Ferretti, A., C. Prati, and F. Rocca, 2001. Permanent scatterers in SAR interferometry, *Geoscience and Remote Sensing, IEEE Transactions on*, *39*(1), 8-20, doi:10.1109/36.898661.

Ferretti, A., A. Fumagalli, F. Novali, C. Prati, F. Rocca, and A. Rucci, 2011. A New Algorithm for Processing Interferometric Data-Stacks: SqueeSAR, *Geoscience and Remote Sensing, IEEE Transactions on*, *49*(9), 3460-3470, doi:10.1109/tgrs.2011.2124465.

Fornaro, G., Verde, S., Reale, D., Pauciullo, A., 2015. CAESAR: An Approach Based on Covariance Matrix Decomposition to Improve Multibaseline-Multitemporal Interferometric SAR Processing. Geoscience and Remote Sensing, IEEE Transactions on 53 (4), 2050–2065. doi:10.1109/TGRS.2014.2352853.

Gomba, G., A. Parizzi, F. D. Zan, M. Eineder, and R. Bamler, 2016. Toward Operational Compensation of Ionospheric Effects in SAR Interferograms: The Split-Spectrum Method, *IEEE Transactions on Geoscience and Remote Sensing*, *54*(3), 1446-1461, doi:10.1109/TGRS.2015.2481079.

Guarnieri, A. M., and S. Tebaldini, 2007. Hybrid Cramér–Rao bounds for crustal displacement field estimators in SAR interferometry, *Signal Processing Letters, IEEE*, *14*(12), 1012-1015, doi:10.1109/LSP.2007.904705.

Guarnieri, A. M., and S. Tebaldini, 2008. On the exploitation of target statistics for SAR interferometry applications, *Geoscience and Remote Sensing, IEEE Transactions on*, *46*(11), 3436-3443, doi:10.1109/TGRS.2008.2001756.

Hanssen, R. F., 2001. *Radar interferometry: data interpretation and error analysis*, Kluwer Academic Pub, Dordrecht, Netherlands.

Hetland, E., P. Musé, M. Simons, Y. Lin, P. Agram, and C. DiCaprio, 2012. Multiscale InSAR time series (MInTS) analysis of surface deformation, *Journal of Geophysical Research: Solid Earth*, *117*(B2), doi:10.1029/2011JB008731.

Hooper, A., H. Zebker, P. Segall, and B. Kampes, 2004. A new method for measuring deformation on volcanoes and other natural terrains using InSAR persistent scatterers, *Geophysical Research Letters*, *31*(23), L23611, doi:10.1029/2004GL021737.

Hooper, A., P. Segall, and H. Zebker, 2007. Persistent scatterer interferometric synthetic aperture radar for crustal deformation analysis, with application to Volcán Alcedo, Galápagos, *Journal of Geophysical Research: Solid Earth*, *112*(B7), doi:10.1029/2006JB004763.

Hussain, E., A. Hooper, T. J. Wright, R. J. Walters, and D. P. S. Bekaert, 2016. Interseismic strain accumulation across the central North Anatolian Fault from iteratively unwrapped InSAR measurements, *Journal of Geophysical Research: Solid Earth, 121*(12), 9000-9019, doi:10.1002/2016JB013108.

Jolivet, R., R. Grandin, C. Lasserre, M. P. Doin, and G. Peltzer, 2011. Systematic InSAR tropospheric phase delay corrections from global meteorological reanalysis data, *Geophysical Research Letters*, 38(17), L17311, doi:10.1029/2011GL048757.

Jolivet, R., P. S. Agram, N. Y. Lin, M. Simons, M. P. Doin, G. Peltzer, and Z. Li, 2014. Improving InSAR geodesy using global atmospheric models, *Journal of Geophysical Research: Solid Earth*, *119*(3), 2324-2341, doi:10.1002/2013JB010588.

Lanari, R., O. Mora, M. Manunta, J. J. Mallorquí, P. Berardino, and E. Sansosti (2004), A small-baseline approach for investigating deformations on full-resolution differential SAR interferograms, *Geoscience and Remote Sensing, IEEE Transactions on*, *42*(7), 1377-1386, doi:10.1109/TGRS.2004.828196.

Lauknes, T. R., H. A. Zebker, and Y. Larsen, 2011. InSAR Deformation Time Series Using an L_1-Norm Small-Baseline Approach, IEEE Transactions on Geoscience and Remote Sensing, 49(1), 536-546, doi:10.1109/TGRS.2010.2051951.

Li, Z., E. Fielding, P. Cross, and R. Preusker, 2009. Advanced InSAR atmospheric correction: MERIS/MODIS combination and stacked water vapour models, *International Journal of Remote Sensing*, *30*(13), 3343-3363, doi:10.1080/01431160802562172.

Liang, C., Z. Liu, E. J. Fielding, and R. Bürgmann, 2018. InSAR Time Series Analysis of L-Band Wide-Swath SAR Data Acquired by ALOS-2, *IEEE Transactions on Geoscience and Remote Sensing, 56*(8), 4492-4506, doi:10.1109/TGRS.2018.2821150.

Lin, Y. n. N., M. Simons, E. A. Hetland, P. Muse, and C. DiCaprio, 2010. A multiscale approach to estimating topographically correlated propagation delays in radar interferograms, *Geochemistry, Geophysics, Geosystems*, *11*(9), doi:10.1029/2010GC003228.

Lohman, R. B., and M. Simons, 2005. Some thoughts on the use of InSAR data to constrain models of surface deformation: Noise structure and data downsampling, *Geochemistry, Geophysics, Geosystems, 6*(1), doi:10.1029/2004GC000841.

López-Quiroz, P., M.-P. Doin, F. Tupin, P. Briole, and J.-M. Nicolas, 2009. Time series analysis of Mexico City subsidence constrained by radar interferometry, *Journal of Applied Geophysics*, *69*(1), 1-15, doi:10.1016/j.jappgeo.2009.02.006.

Morrison, K., J. C. Bennett, M. Nolan, and R. Menon, 2011. Laboratory Measurement of the DInSAR Response to Spatiotemporal Variations in Soil Moisture, *IEEE Transactions on Geoscience and Remote Sensing*, *49*(10), 3815-3823, doi:10.1109/TGRS.2011.2132137.

Onn, F., and H. A. Zebker, 2006. Correction for interferometric synthetic aperture radar atmospheric phase artifacts using time series of zenith wet delay observations from a GPS network, *Journal of Geophysical Research: Solid Earth*, *111*(B9), n/a-n/a, doi:10.1029/2005JB004012.

Parizzi, A., X. Cong, and M. Eineder, 2009. First Results from Multifrequency Interferometry. A comparison of different decorrelation time constants at L, C, and X Band, *ESA Scientific Publications* (SP-677), 1-5.

Pepe, A., and R. Lanari, 2006. On the extension of the minimum cost flow algorithm for phase unwrapping of multitemporal differential SAR interferograms, *Geoscience and Remote Sensing, IEEE Transactions on*, *44*(9), 2374-2383, doi:10.1109/TGRS.2006.873207.

Pepe, A., A. B. Ortiz, P. R. Lundgren, P. A. Rosen, and R. Lanari (2011), The Stripmap–ScanSAR SBAS Approach to Fill Gaps in Stripmap Deformation Time Series With ScanSAR Data, *IEEE Transactions on Geoscience and Remote Sensing*, *49*(12), 4788-4804, doi:10.1109/TGRS.2011.2167979.

Pepe, A., Y. Yang, M. Manzo, and R. Lanari, 2015. Improved EMCF-SBAS Processing Chain Based on Advanced Techniques for the Noise-Filtering and Selection of Small Baseline Multi-Look DInSAR Interferograms, *Geoscience and Remote Sensing, IEEE Transactions on*, *PP*(99), 1-24, doi:10.1109/TGRS.2015.2396875.

Perissin, D., and T. Wang, 2012. Repeat-pass SAR interferometry with partially coherent targets, *Geoscience and Remote Sensing, IEEE Transactions on*, *50*(1), 271-280, doi:10.1109/tgrs.2011.2160644.

Rocca, F., 2007. Modeling interferogram stacks, *IEEE Transactions on Geoscience and Remote Sensing*, *45*(10), 3289-3299, doi:10.1109/TGRS.2007.902286.

Rosen, P. A., S. Hensley, G. Peltzer, and M. Simons, 2004. Updated repeat orbit interferometry package released, *Eos Trans. AGU*, *85*(5), 47-47, doi:10.1029/2004EO050004.

Rosen, P. A., E. Gurrola, G. F. Sacco, and H. Zebker, 2012. The InSAR scientific computing environment, paper presented at EUSAR 2012, 23-26 April 2012.

Rodriguez, E., and J. Martin, 1992. Theory and design of interferometric synthetic aperture radars, paper presented at IEE Proceedings F (Radar and Signal Processing), IET, doi:10.1049/ip-f-2.1992.0018.

Rousseeuw, P. J., and M. Hubert, 2011. Robust statistics for outlier detection, *Wiley Interdisciplinary Reviews: Data Mining and Knowledge Discovery*, 1(1), 73-79, doi:10.1002/widm.2.

Samiei-Esfahany, S., J. E. Martins, F. v. Leijen, and R. F. Hanssen, 2016. Phase Estimation for Distributed Scatterers in InSAR Stacks Using Integer Least Squares Estimation, *IEEE Transactions on Geoscience and Remote Sensing*, *54*(10), 5671-5687, doi:10.1109/TGRS.2016.2566604.

Schmidt, D. A., and R. Bürgmann, 2003. Time-dependent land uplift and subsidence in the Santa Clara valley, California, from a large interferometric synthetic aperture radar data set, *Journal of Geophysical Research: Solid Earth*, *108*(B9), doi:10.1029/2002JB002267.

Seymour, M. S., and I. G. Cumming, 1994. Maximum likelihood estimation for SAR interferometry, paper presented at Geoscience and Remote Sensing Symposium, 1994. IGARSS '94, 8-12 Aug 1994, doi:10.1109/IGARSS.1994.399711.

Sudhaus, H., and S. Jónsson (2009), Improved source modelling through combined use of InSAR and GPS under consideration of correlated data errors: application to the June 2000 Kleifarvatn earthquake, Iceland, *Geophysical Journal International*, *176*(2), 389-404, doi:10.1111/j.1365-246X.2008.03989.x.

Tong, X., D. T. Sandwell, and B. Smith-Konter, 2013. High-resolution interseismic velocity data along the San Andreas Fault from GPS and InSAR, *Journal of Geophysical Research: Solid Earth*, *118*(1), 369-389, doi:10.1029/2012JB009442.

Tough, R. J. A., D. Blacknell, and S. Quegan, 1995. A Statistical Description of Polarimetric and Interferometric Synthetic Aperture Radar Data, *Proceedings: Mathematical and Physical Sciences*, *449*(1937), 567-589, doi:10.1098/rspa.1995.0059.

Werner, C., U. Wegmüller, T. Strozzi, and A. Wiesmann, 2000. Gamma SAR and interferometric processing software, paper presented at *Proceedings of the ERS-Envisat symposium*, Gothenburg, Sweden.

Xu, X., and D. T. Sandwell (2019), Towards Absolute Phase Recovery with InSAR: Correcting for Earth Tides and Phase Unwrapping Ambiguities, *IEEE Transactions on Geoscience and Remote Sensing*, doi:10.1109/TGRS.2019.2940207.

Yu, C., Z. Li, and N. T. Penna, 2018. Interferometric synthetic aperture radar atmospheric correction using a GPS-based iterative tropospheric decomposition model, *Remote Sensing of Environment*, *204*, 109-121, doi:10.1016/j.rse.2017.10.038.

Zebker, H. A., and J. Villasenor, 1992. Decorrelation in interferometric radar echoes, *Geoscience and Remote Sensing, IEEE Transactions on*, *30*(5), 950-959, doi:10.1109/36.175330.

Computers and Geosciences
Supplementary Information for

Small baseline InSAR time series analysis: Unwrapping error correction and noise reduction

Zhang Yunjun[a], Heresh Fattahi[b], Falk Amelung[a]

[a] Rosenstiel School of Marine and Atmospheric Science, University of Miami, Miami, Florida, USA

[b] Jet Propulsion Laboratory, California Institute of Technology, Pasadena, California, USA

Content of this file

S1. Supplemental figures and tables

This section provides figures S1 to S9 and table S1. Fig. S1 shows the standard deviation of the interferometric phase as a function of the spatial coherence and number of looks. Fig. S2 demonstrates the performance of four weighting functions in different temporal decorrelation settings using the mean RMSE of 10,000 realizations of the inverted phase time-series as a function of the number of looks. Fig. S3 demonstrates the simulation of the unwrapped interferogram for unwrapping error correction with the bridging method, considering the ground deformation, tropospheric turbulence, phase ramps and decorrelation noise. Fig. S4 shows the output percentage of interferograms with unwrapping errors as a function of the LASSO parameter to find its suitable value range. Fig. S5 demonstrates the necessity of adding the step function during the topographic residual correction in the presence of displacement jump using both simulated and read data. Fig. S6 shows the coherence matrix of Sentinel-1 dataset for GPS stations within Sierra Negra. Fig. S7 shows the estimated residual phase time-series. Fig. S8 shows the coherence-based network modification for the Sentinel-1 data used in the discussion of the network redundancy in section 6.3. Fig. S9 compares the displacement time-series from the approaches in GIAnT and MintPy with and without unwrapping error correction and weighted network inversion. Table S1 summaries the information of SAR data used in the paper and their configurations for InSAR stack processing.

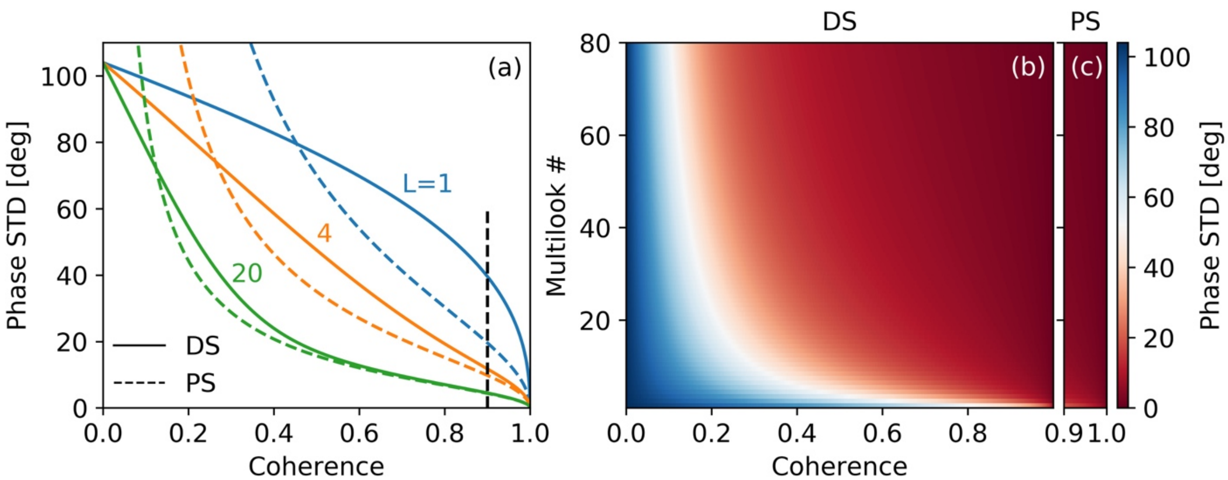

Figure S1. Phase standard deviation versus spatial coherence for PS and DS. Related to equation (6). (a) Standard deviation of interferometric phase as function of coherence for DS (solid lines) and PS (dashed lines) with 1, 4 and 20 looks. The black dashed line marks the effective boundary for PS ($0.9 < |\gamma| \leq 1$). (b) Lookup table to convert spatial coherence to phase standard deviation for number of looks in [1, 80].

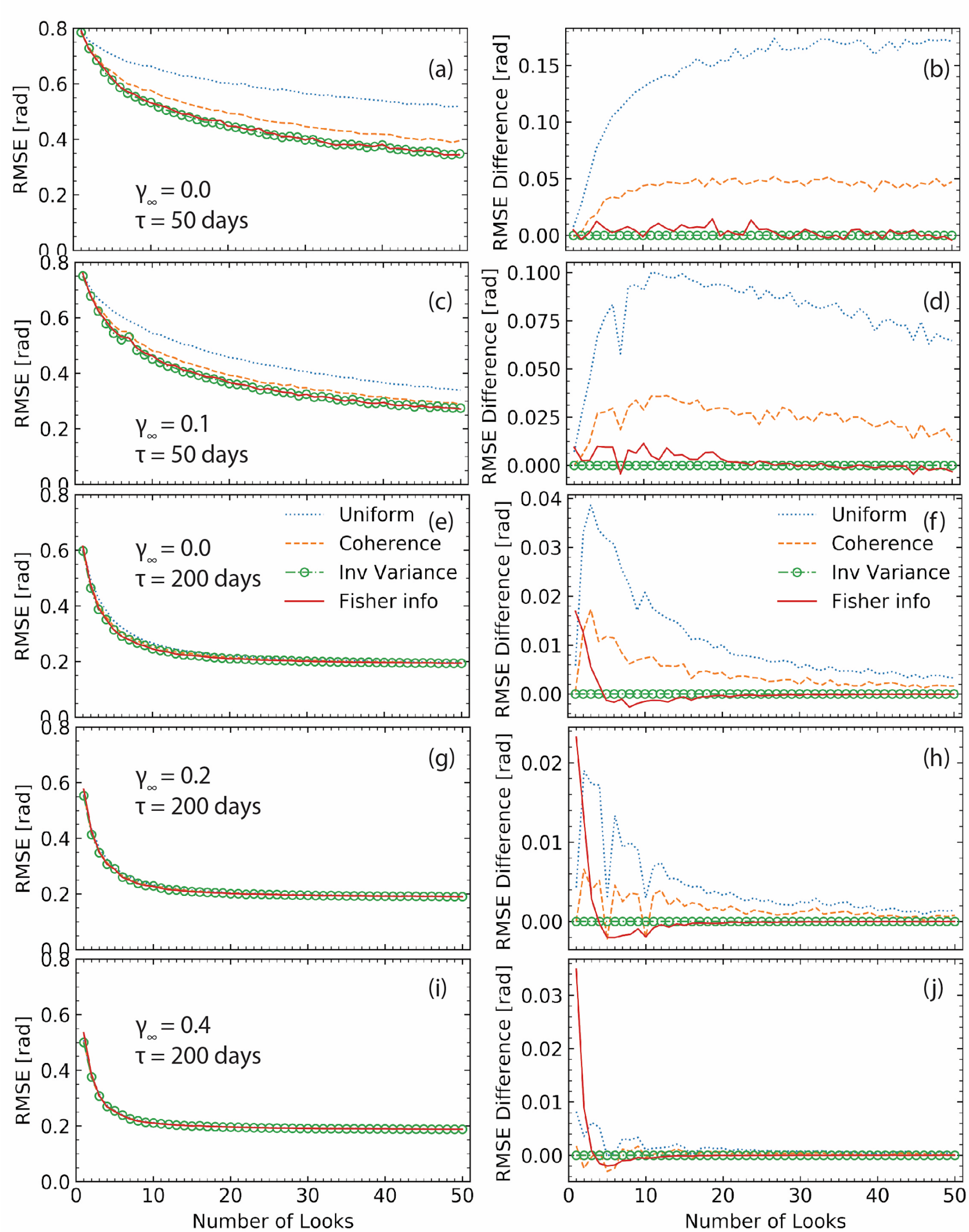

Figure S2. Performance indicator for four weighting functions based on (left panel) the mean RMSE of 10,000 realizations of inverted phase time-series as a function of the number of looks. Related to Fig. 1, which uses $\gamma_\infty = 0.0$ and $\tau = 200$ days. Right panel: same as left panel but shown in differential RMSE with respect to inverse-variance weighting. From top to bottom for different temporal decorrelation settings.

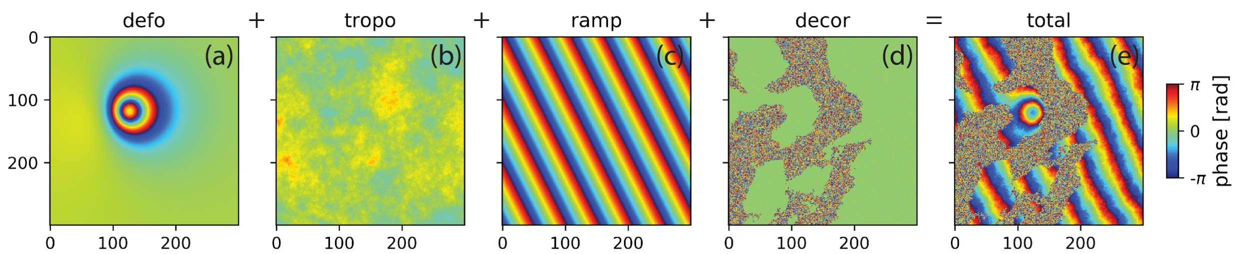

Figure S3. Simulate interferogram for unwrapping error correction with the bridging method. Related to Fig. 2. We consider an area of 300 by 300 pixels with spatial resolution of 62 m in both directions, illustrated by radar echoes in a Sentinel-1-like geometry in descending orbit (with an incidence angle of 34 deg and heading angle of -168 deg). (a) Deformation phase caused by a Mogi source (x = 120 row, y = 120 col, z = 2 km under the free surface with a volume change of 10^6 m^3), (b) tropospheric turbulence modeled as an isotropic two-dimensional surface with a power law behavior (the multiplier of spectrum amplitude p0=1e-3, assuming a flat area without stratified tropospheric delay; Hanssen, 2001), (c) phase ramp modeled as a linear surface, and (d) simulated decorrelation noise (see section S3). The water body mask is rescaled from the real DEM in western Kyushu, Japan. We specify the spatial coherence of 0.6 and 0.001 for pixels on land and water respectively with the number of looks of 15 by 5.

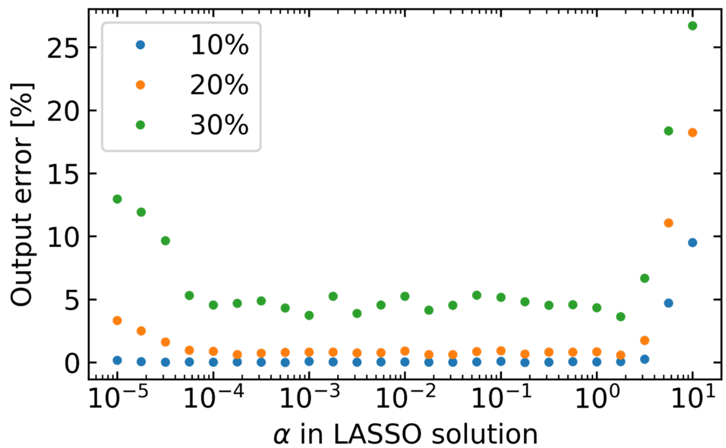

Figure S4. Simulation for the optimal LASSO trade-off parameter α. Related to equation (11) in section 3.2. Mean output percentage of 100 realization of interferograms with unwrapping errors after correction as a function of the nonnegative α value for different input percentage of interferograms with unwrapping errors. The network of interferograms is the same as Fig. 4a. The simulation result shows that any number of α in [10^{-4}, 10^{0}] works. We choose 10^{-2} as default value.

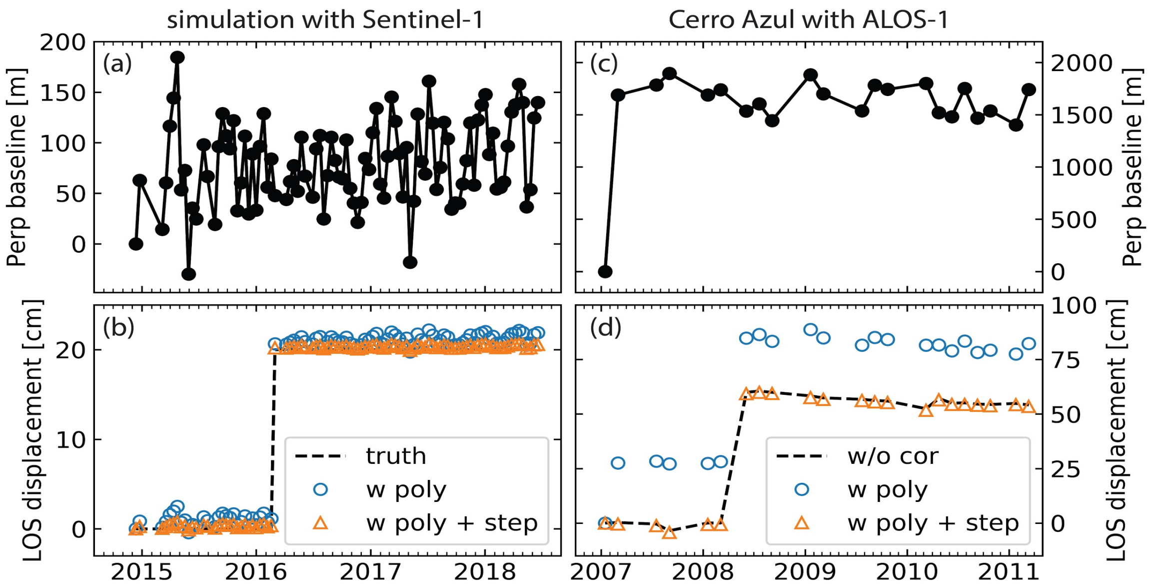

Figure S5. Illustration of the step function in topographic residual correction in presence of displacement jumps. Related to equation (13) in section 4.8. (a and b) Perpendicular baseline history (from the Sentinel-1 data of section 5) and an arbitrary displacement time-series using simulated data (with a permanent displacement jump at 1 March 2016 with a magnitude of 20 cm, shown as the dashed black line in (b), in addition to the topographic residual contribution from a DEM error of 50 m). Blue empty circles and orange triangles represent displacement time-series after topographic residual correction assuming quadratic model without and with a step function, respectively. (c and d) Same as (a and b) but (i) using ALOS-1 data for one pixel on Cerro Azul located at [W91.270°, S0.928°] and (ii) the black dashed line for the displacement time-series without topographic residual correction. In both simulated and real data, the disagreement between the low-frequency quadratic model and the high-frequency displacement jump leads to biased estimation of the topographic residual (Du et al., 2007) and adding a step function could effectively eliminate this estimation bias. This estimation bias is amplified in the first ALOS-1 acquisition by its large perpendicular baseline (the difference between black dashed line and the blue empty circles in (d)).

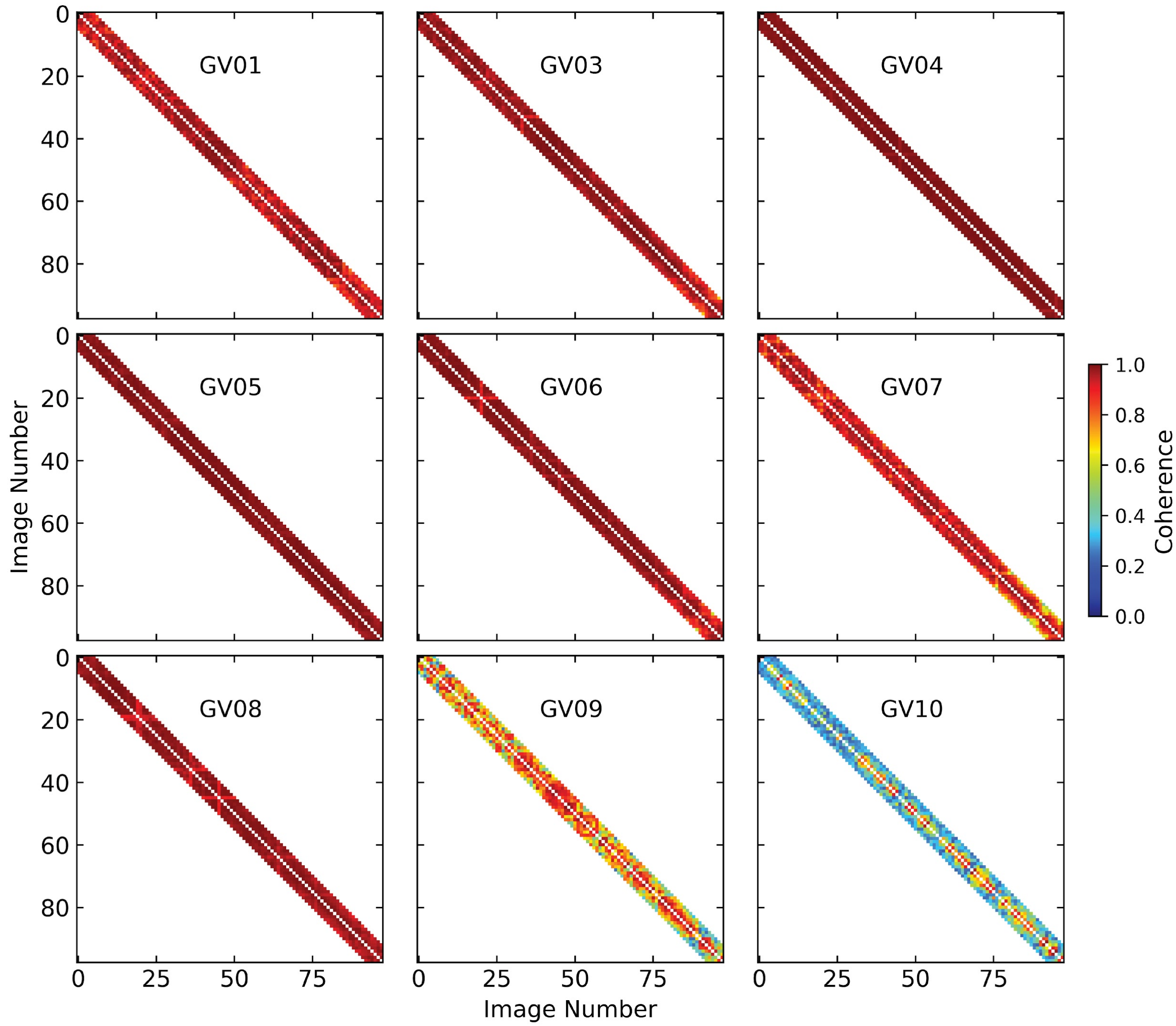

Figure S6. Coherence matrix of Sentinel-1 dataset for GPS stations within Sierra Negra caldera. Related to Fig. 8 in section 5.1. Both X and Y axis indicate the number of SAR acquisitions. Station GV10 is located in a densely vegetated area outside the caldera on the rim, resulting in fast decorrelation with low spatial coherence on interferograms with more than 2 lags.

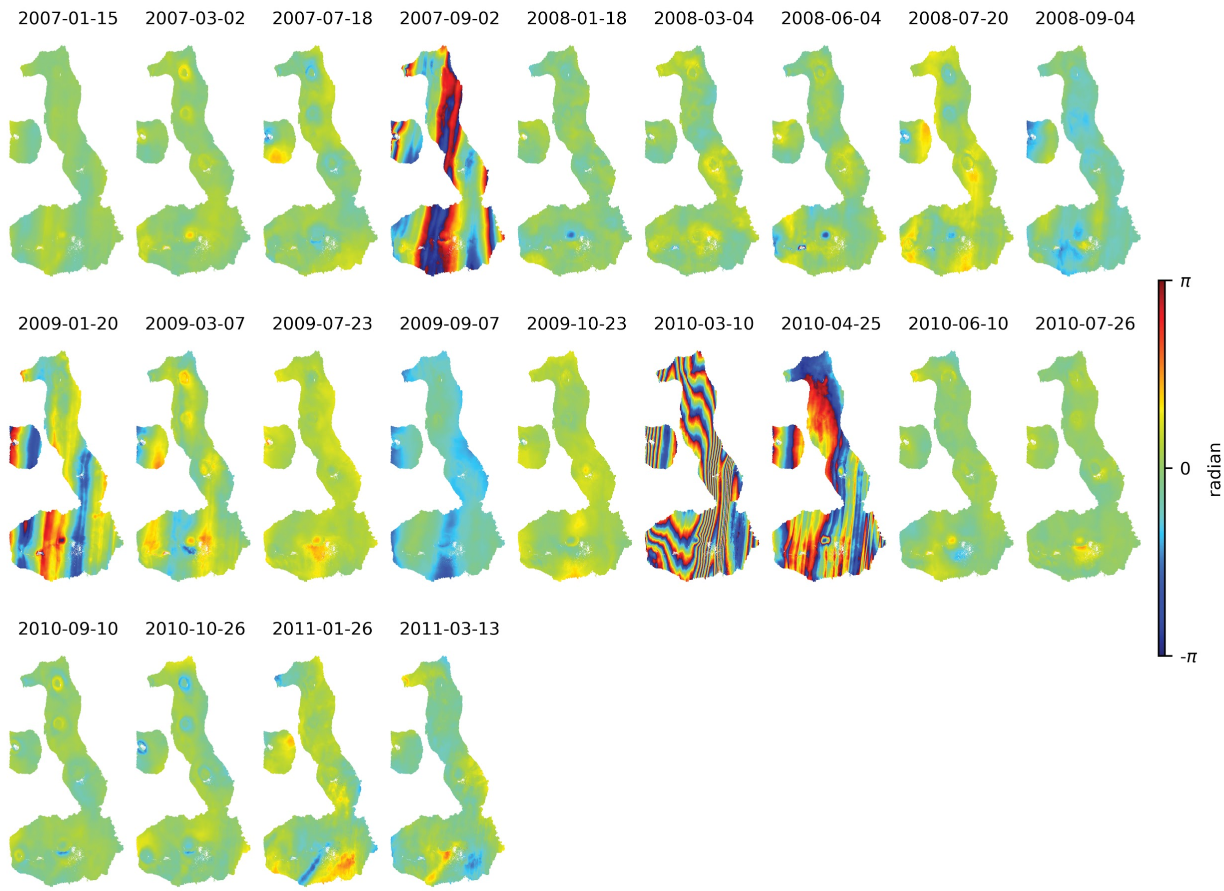

Figure S7. The estimated residual phase time-series $\hat{\phi}_{resid}$ of ALOS-1 dataset. Related to equation (13-14) in section 4.7 and Fig. 12 in section 5.4. A quadratic phase ramp has been estimated and removed from each acquisition. This is used in equation (14) to calculate the residual phase RMS value. Phases on 2 September 2007, 10 March 2010 and 25 April 2010 are severely contaminated by ionospheric streaks and are automatically identified as outliers. Phase on 20 January 2009 is contaminated by ionosphere also but is not identified as outlier due to its relatively small magnitude.

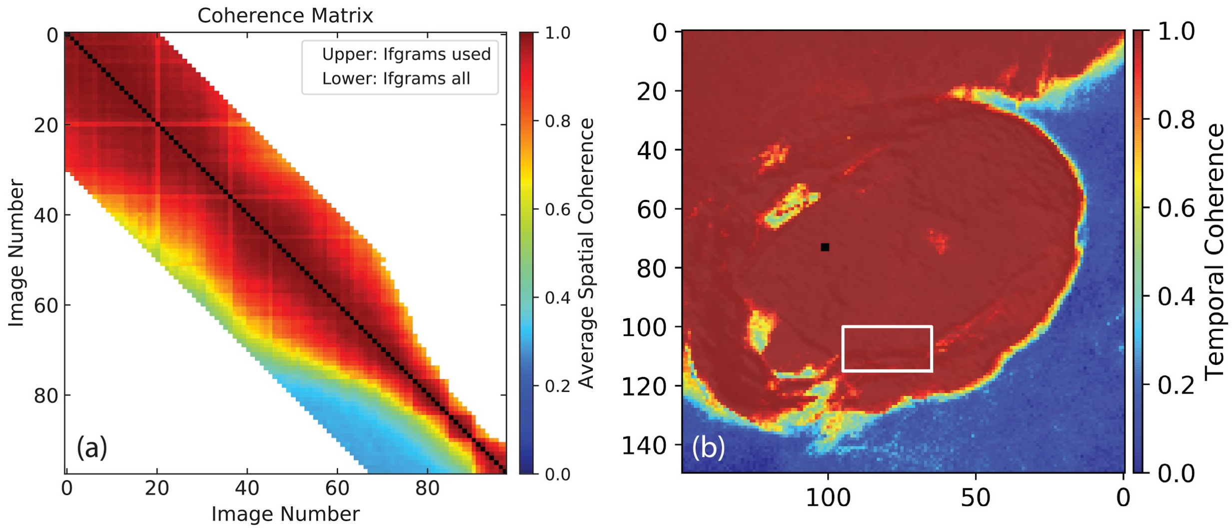

Figure S8. Coherence-based network modification for Sentinel-1 data used in section 6.3 in Sierra Negra. Related to Fig. 14 in section 6.3. (a) Coherence matrix of the customized area of interest along the trap door fault within Sierra Negra caldera (marked by the white rectangle in (b)). A network of interferograms with 30 sequential connections (2475 in total) are generated from 98 SAR acquisitions, as shown in the lower triangle. The upper triangle shows the interferogram kept after the network modification. A maximum of 20 connections are shown in Fig. 14 only. (b) Temporal coherence of the network inversion from the interferogram stack with a maximum of 20 connections.

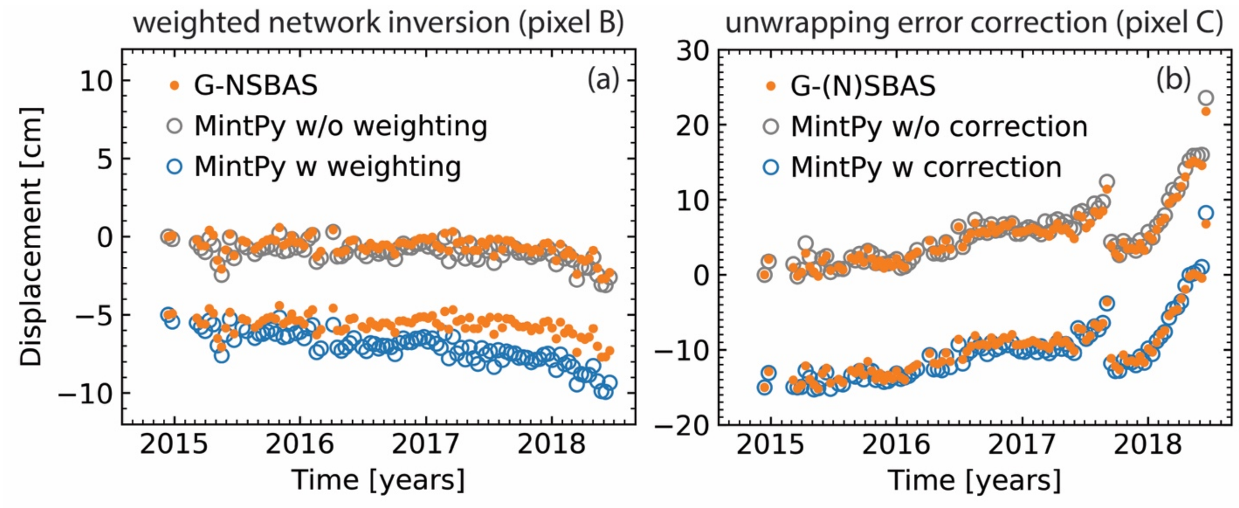

Figure S9. Impact of (a) weighted network inversion and (b) unwrapping error correction on the displacement time-series. Related to Fig. 16 in section 6.5. The comparison within (a) shows that the difference on pixel B (Alcedo's flank) between MintPy and G-NSBAS is caused by the weighting during the network inversion. The comparison within (b) shows that the difference on pixel C (Fernandina's crater) between MintPy and G-(N)SBAS is caused by the unwrapping error correction.

Table S1. SAR dataset information with parameters used in InSAR stack processing

Satellite	ALOS-1	Sentinel-1A/B
Orbit direction	Ascending	Descending
Track number	133	128 (swath 1 & 2)
Start / end date (# of acquisitions)	2007-01-15 / 2011-03-13 (22)	2014-12-13 / 2018-06-19 (98)
Network selection criteria (# of Interferograms)	$B_{temp} \leq 1800$ days $B_{\perp} \leq 1800$ m (228)	Sequential with 5 connections (475)
# of looks in range / azimuth direction	8×16	15×5
Ground pixel size in range / azimuth direction (m)	60×51	62×70
InSAR Processor	ROI_PAC	ISCE
Phase Unwrapping	SNAPHU	SNAPHU

S2. Design matrices

This section shows examples to generate the design matrices used in the software. A demo set of $N = 8$ SAR images acquired at $[t_1,...,t_8]$ is used as the example. A stack of $M = 18$ interferograms is selected using the sequential method with 3 connections. An earthquake or volcanic eruption event occurred between t_6 and t_7 (red dashed line), which caused a permanent ground displacement offset.

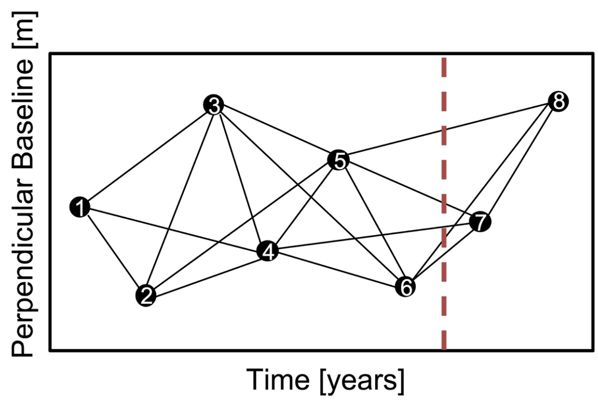

Figure S10. *Network configuration of the demo dataset. Red dashed line marks the time of a displacement offset due to an earthquake or volcanic eruption.*

S2.1 Network inversion

To generate the design matrix $\boldsymbol{A}$ for network inversion used in equation (1) in section 2.1, we first generate an $M \times N$ matrix. For each row, it consists -1, 0 and 1 with -1 for the reference acquisition, 1 for the secondary acquisition and 0 for the rest. Due to the relative nature of InSAR measurement, the phase on the reference date (the first date by default) cannot be resolved, thus, we can only solve $[\phi^2, ..., \phi^N]$ instead of $[\phi^1, ..., \phi^N]$ and the corresponding column (the first column by default) is eliminated in the design matrix $\boldsymbol{A}$, which results in size of $M \times (N - 1)$.

$$
\boldsymbol{A} = \left[\begin{array}{c|ccccccc}
-1 & 1 & 0 & 0 & 0 & 0 & 0 & 0 \\
-1 & 0 & 1 & 0 & 0 & 0 & 0 & 0 \\
-1 & 0 & 0 & 1 & 0 & 0 & 0 & 0 \\
0 & -1 & 1 & 0 & 0 & 0 & 0 & 0 \\
0 & -1 & 0 & 1 & 0 & 0 & 0 & 0 \\
0 & -1 & 0 & 0 & 1 & 0 & 0 & 0 \\
0 & 0 & -1 & 1 & 0 & 0 & 0 & 0 \\
0 & 0 & -1 & 0 & 1 & 0 & 0 & 0 \\
0 & 0 & -1 & 0 & 0 & 1 & 0 & 0 \\
0 & 0 & 0 & -1 & 1 & 0 & 0 & 0 \\
0 & 0 & 0 & -1 & 0 & 1 & 0 & 0 \\
0 & 0 & 0 & -1 & 0 & 0 & 1 & 0 \\
0 & 0 & 0 & 0 & -1 & 1 & 0 & 0 \\
0 & 0 & 0 & 0 & -1 & 0 & 1 & 0 \\
0 & 0 & 0 & 0 & -1 & 0 & 0 & 1 \\
0 & 0 & 0 & 0 & 0 & -1 & 1 & 0 \\
0 & 0 & 0 & 0 & 0 & -1 & 0 & 1 \\
0 & 0 & 0 & 0 & 0 & 0 & -1 & 1
\end{array}\right] \qquad \text{(S1)}
$$

S2.2 Phase closure of interferograms triplets

Design matrix $\boldsymbol{C}$ describe the combination of interferograms to form the triplets used in equation (10) in section 3.2 for the phase closure unwrapping error correction. An example of $\boldsymbol{C}$ is shown below based on the demo network with number of triplets $T = 16$.

[1 -1 0 1 0 0 0 0 0 0 0 0 0 0 0 0 0 0]

[1 0 -1 0 1 0 0 0 0 0 0 0 0 0 0 0 0 0]

[0 1 -1 0 0 0 1 0 0 0 0 0 0 0 0 0 0 0]

[0 0 0 1 -1 0 1 0 0 0 0 0 0 0 0 0 0 0]

[0 0 0 1 0 -1 0 1 0 0 0 0 0 0 0 0 0 0]

[0 0 0 0 1 -1 0 0 0 1 0 0 0 0 0 0 0 0]

[0 0 0 0 0 0 1 -1 0 1 0 0 0 0 0 0 0 0]

$$
\begin{aligned}
\boldsymbol{C} = \; & [0\ 0\ 0\ 0\ 0\ 0\ 1\ 0\ {-1}\ 0\ 1\ 0\ 0\ 0\ 0\ 0\ 0\ 0] \\
& [0\ 0\ 0\ 0\ 0\ 0\ 0\ 1\ {-1}\ 0\ 0\ 0\ 1\ 0\ 0\ 0\ 0\ 0] \\
& [0\ 0\ 0\ 0\ 0\ 0\ 0\ 0\ 0\ 1\ {-1}\ 0\ 1\ 0\ 0\ 0\ 0\ 0] \\
& [0\ 0\ 0\ 0\ 0\ 0\ 0\ 0\ 0\ 1\ 0\ {-1}\ 0\ 1\ 0\ 0\ 0\ 0] \\
& [0\ 0\ 0\ 0\ 0\ 0\ 0\ 0\ 0\ 0\ 1\ {-1}\ 0\ 0\ 0\ 1\ 0\ 0] \\
& [0\ 0\ 0\ 0\ 0\ 0\ 0\ 0\ 0\ 0\ 0\ 0\ 1\ {-1}\ 0\ 1\ 0\ 0] \\
& [0\ 0\ 0\ 0\ 0\ 0\ 0\ 0\ 0\ 0\ 0\ 0\ 1\ 0\ {-1}\ 0\ 1\ 0] \\
& [0\ 0\ 0\ 0\ 0\ 0\ 0\ 0\ 0\ 0\ 0\ 0\ 0\ 1\ {-1}\ 0\ 0\ 1] \\
& [0\ 0\ 0\ 0\ 0\ 0\ 0\ 0\ 0\ 0\ 0\ 0\ 0\ 0\ 0\ 1\ {-1}\ 1]
\end{aligned}
\qquad \text{(S2)}
$$

S2.3 Topographic residual correction

Design matrix $\boldsymbol{G}$ is used in equation (13) for topographic residual correction in section 4.8. It is in size of $N \times (1 + N_{poly} + N_{step})$, where N_{poly} is the user-defined polynomial order N_{poly} (2 by default), N_{step} is the number of Heaviside step functions (0 by default) describing offsets at specific prior selected times. An example of $\boldsymbol{G}$ is shown below based on the demo network.

$$
\boldsymbol{G} = \begin{bmatrix}
\frac{4\pi}{\lambda}\frac{B_\perp^1}{r\sin(\theta)} & 1 & (t_1 - t_1) & \frac{(t_1-t_1)^2}{2} & 0 \\
\frac{4\pi}{\lambda}\frac{B_\perp^2}{r\sin(\theta)} & 1 & (t_2 - t_1) & \frac{(t_2-t_1)^2}{2} & 0 \\
\frac{4\pi}{\lambda}\frac{B_\perp^3}{r\sin(\theta)} & 1 & (t_3 - t_1) & \frac{(t_3-t_1)^2}{2} & 0 \\
\frac{4\pi}{\lambda}\frac{B_\perp^4}{r\sin(\theta)} & 1 & (t_4 - t_1) & \frac{(t_4-t_1)^2}{2} & 0 \\
\frac{4\pi}{\lambda}\frac{B_\perp^5}{r\sin(\theta)} & 1 & (t_5 - t_1) & \frac{(t_5-t_1)^2}{2} & 0 \\
\frac{4\pi}{\lambda}\frac{B_\perp^6}{r\sin(\theta)} & 1 & (t_6 - t_1) & \frac{(t_6-t_1)^2}{2} & 0 \\
\frac{4\pi}{\lambda}\frac{B_\perp^7}{r\sin(\theta)} & 1 & (t_7 - t_1) & \frac{(t_7-t_1)^2}{2} & 1 \\
\frac{4\pi}{\lambda}\frac{B_\perp^8}{r\sin(\theta)} & 1 & (t_8 - t_1) & \frac{(t_8-t_1)^2}{2} & 1
\end{bmatrix}
\qquad \text{(S3)}
$$

Then equation (13) can be formed as a linear system with *N* equations as below:

$$\hat{\phi} - \hat{\phi}_{tropo} = \boldsymbol{G}X + \phi_{resid} \quad \text{(S4)}$$

where $X = [z_\varepsilon, c_0, c_1, c_2, s_7]^T$ is the vector of unknown parameters, $\hat{\phi}$, $\hat{\phi}_{tropo}$ and ϕ_{resid} are the $N \times 1$ inverted raw phase time-series, estimated tropospheric delay time-series and residual phase time-series, respectively. We apply the least squares estimation to obtain the solution as:

$$\hat{X} = (\boldsymbol{G}^T\boldsymbol{G})^{-1}\boldsymbol{G}^T(\hat{\phi} - \hat{\phi}_{tropo}) \quad \text{(S5)}$$

$$\hat{\phi}_{resid} = \hat{\phi} - \hat{\phi}_{tropo} - \boldsymbol{G}\hat{X} \quad \text{(S6)}$$

The estimated residual phase $\hat{\phi}_{resid}$ is used to characterize the noise of phase time-series using equation (14) in section 4.9. The noise-reduced displacement time-series is given as:

$$\phi_{dis}^i = \hat{\phi}^i - \hat{\phi}_{tropo}^i - \frac{-4\pi}{\lambda}\frac{B_\perp^i}{r\sin(\theta)}\hat{z}_\varepsilon \quad \text{(S7)}$$

where $i = 1, \ldots, N$ and $\hat{z}_\varepsilon$ is the estimated DEM error in $\hat{X}$.

S2.4 Average velocity estimation

For each pixel, the average velocity is estimated as $d^i = vt_i + c$, where $d^i = -\frac{\lambda}{4\pi}\phi_{dis}^i$ is the displacement at t_i in meters, v is the unknown velocity and c is the unknown offset. The solution can be obtained using least squares approximation. An example of the design matrix $\boldsymbol{E}$ is shown below based on the demo network.

$$\boldsymbol{E} = \begin{bmatrix} t_1 - t_1 & 1 \\ t_2 - t_1 & 1 \\ t_3 - t_1 & 1 \\ t_4 - t_1 & 1 \\ t_5 - t_1 & 1 \\ t_6 - t_1 & 1 \\ t_7 - t_1 & 1 \\ t_8 - t_1 & 1 \end{bmatrix} \tag{S8}$$

For linear displacement, the uncertainty of the estimated velocity σ_v is given by equation (10) in Fattahi and Amelung (2015) as:

$$\sigma_v = \sqrt{\frac{\sum_{i=1}^{N}(\phi_{dis}^{i} - \hat{\phi}_{dis}^{i})^2}{(N-2)\sum_{i=1}^{N}(t_i - \bar{t})^2}} \tag{S9}$$

where $\hat{\phi}_{dis}^{i}$ is the predicted linear displacement at i_{th} acquisition $\bar{t}$ is the mean value of time in years.

S3. Decorrelation noise simulation

S3.1 Coherence model

We simulate the coherence for a stack of interferograms on one pixel using a decorrelation model with exponential decay for temporal decorrelation. The spatial coherence γ^j of the j_{th} interferogram can be expressed as (Zebker and Villasenor, 1992; Hanssen, 2001; Parizzi et al., 2009):

$$\gamma = \gamma_{geom} \cdot \gamma_{DC} \cdot \gamma_{temporal} \tag{S10}$$

where γ_{geom} represents the geometric decorrelation, γ_{DC} represents the Doppler centroid decorrelation, $\gamma_{temporal}$ represents the temporal decorrelation, given by the equations below. Note that the thermal decorrelation $\gamma_{thermal}$ is served as the instantaneous decorrelation in temporal decorrelation $\gamma_{temporal}$ (Parizzi et al., 2009).

$$\gamma_{geom} = \begin{cases} 1 - \frac{|B_\perp|}{B_\perp^{crit}}, & |B_\perp| \leq B_\perp^{crit} \\ 0, & |B_\perp| > B_\perp^{crit} \end{cases} \tag{S11}$$

$$\gamma_{DC} = \begin{cases} 1 - \frac{|\Delta f_{DC}|}{B_{az}}, & |\Delta f_{DC}| \leq B_{az} \\ 0, & |\Delta f_{DC}| > B_{az} \end{cases} \tag{S12}$$

$$\gamma_{temporal}(t) = (\gamma_{thermal} - \gamma_\infty)e^{-t/\tau} + \gamma_\infty \tag{S13}$$

$$\gamma_{thermal} = \frac{1}{1 - SNR^{-1}} \tag{S14}$$

The critical perpendicular baseline $B_{\perp}^{crit} = \lambda \frac{B_{rg}}{c} R \cdot tan(\theta)$ is the baseline causing a spectral shift equal to the radar bandwidth B_{rg} in range direction (Zebker and Villasenor, 1992; Hanssen, 2001), where λ is the radar wavelength, c is the speed of light, R is the distance between radar antenna and ground target and θ is the incidence angle, *SNR* is the thermal signal-to-noise ratio of radar receiver. τ is the time constant which depends on radar wavelength λ, it's the time for coherence to drop down to 1/*e*, i.e. 0.36, from its initial value (Parizzi et al., 2009; Rocca, 2007). γ_∞ is the long-term coherence, or minimum attainable coherence value, which converged over time, usually with high values in urban area and low values in vegetated area. Note that this model does not consider the seasonal behavior of temporal decorrelation, volume decorrelation, and processing-induced decorrelation. For a given set of SAR acquisitions, the geometric and Doppler centroid decorrelation is almost constant among all pixels. All parameters are deployed with typical parameters of Sentinel-1 SAR sensor.

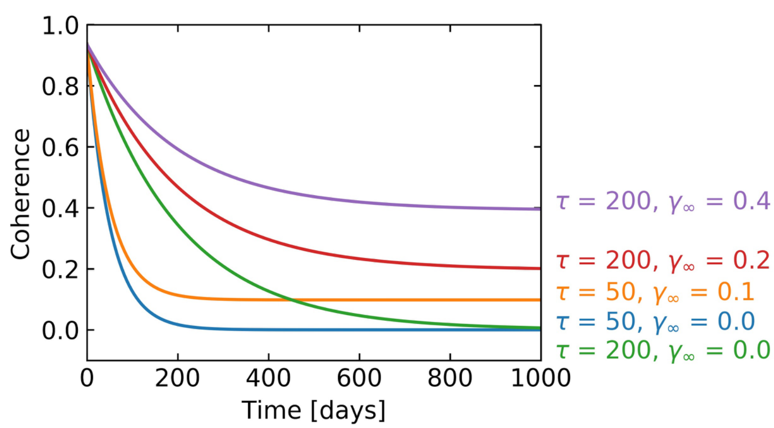

Figure S11. *Simulated coherence as a function of temporal baseline, color coded by different τ and γ_∞ settings used in Fig. S2.*

S3.2 Simulate decorrelation noise from coherence

For distributed scatterers (DS) in natural, vegetated terrain the interferometric phase exhibits highly unpredictable speckle characteristics. Its phase can be appropriately modeled by a random process, complex, stationary, circular Gaussian process in the case of SAR image. Applying the central limit theorem, the probability density function $pdf(\Delta\phi)$ of interferometric phase is obtained as (equation (66) from Tough et al., 1995; equation (4.2.23) from Hanssen, 2001):

$$pdf(\Delta\phi) = \frac{(1-|\gamma|^2)^L}{2\pi}\left\{\frac{\Gamma(2L-1)}{[\Gamma(L)]^2 2^{2(L-1)}} \times [\frac{(2L-1)\beta}{(1-\beta^2)^{L+\frac{1}{2}}}(\frac{\pi}{2} + arcsin\beta) + \frac{1}{(1-\beta^2)^L}] + D\right\} \qquad \text{(S15)}$$

$$D = \frac{1}{2(L-1)}\sum_{r=0}^{L-2}\frac{\Gamma(L-\frac{1}{2})}{\Gamma(L-\frac{1}{2}-r)}\frac{\Gamma(L-1-r)}{\Gamma(L-1)}\frac{1+(2r+1)\beta^2}{(1-\beta^2)^{r+2}}$$

where $\beta = |\gamma|cos(\Delta\phi - \Delta\phi_0)$, expected interferometric phase $\Delta\phi_0 = E\{\Delta\phi\}$, gamma function $\Gamma(L) = \int_0^\infty t^{L-1}e^{-t}dt\, , for\ L \in R$ and D a finite summation term. Note that D vanishes for single-look datasets (L=1).

The 10,000 realizations/samples of decorrelation noise of each interferogram (used in section 2.4) is simulated by generating a distribution given by equation (S15) with corresponding coherence γ and number of looks L. One example with $\gamma = 0.1$ and $L = 9 \times 3$ is shown in Fig. S12.

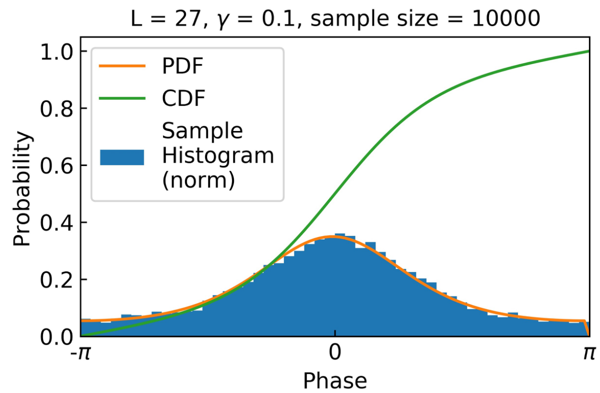

Figure S12. *Sampling the decorrelation noise based on phase PDF of distributed scatterers. Blue bars: normalized histogram of sampled decorrelation noises. Orange and green solid line: phase PDF and cumulative distribution function.*

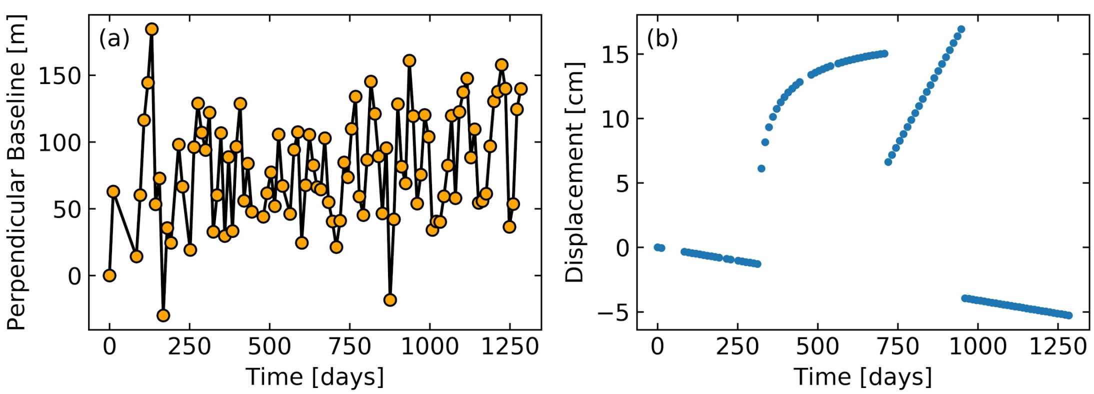

Figure S13. *Time-series configuration for simulation. (a) Perpendicular baseline history from the 98 Sentinel-1 images of section 5. (b) Specified time-dependent displacement used in section 2.4 and 3.2.*

S4. Additional software features

S4.1 Customized workflow beyond `smallbaselineApp.py`

Most scripts in MintPy are stand-alone (summarized in Table S4). Users can apply any phase correction at any time to evaluate the impact. Fig. S14 shows an example, where we use individual scripts (link on GitHub) to compare velocities estimated from displacement time-series with different tropospheric delay correction methods on Alcedo volcano.

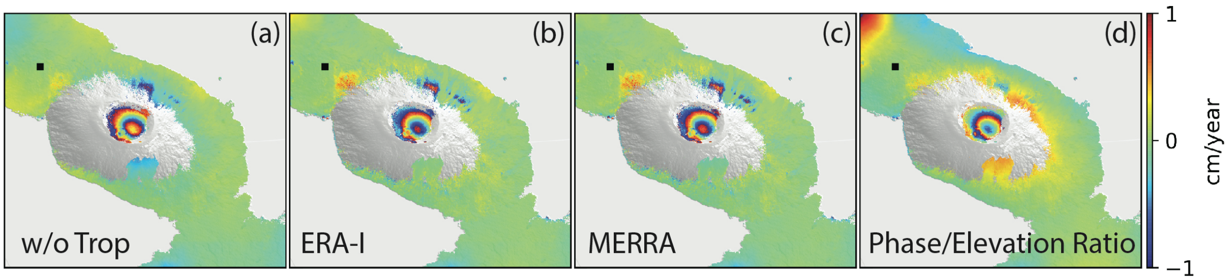

Figure S14. *Deformation velocity maps on Alcedo volcano from Sentinel-1 (a) without tropospheric correction, with tropospheric correction using (b) ERA-Interim, (c) MERRA-2 and (d) the empirical phase-elevation ratio method.*

Table S4. *Stand-alone scripts in MintPy*

`add.py`	Generate the sum of multiple input files
`asc_desc2horz_vert.py`	Project ascending and descending displacement in LOS direction to horizontal and vertical direction
`dem_error.py`	DEM error (topographic residual) correction
`diff.py`	Generate the difference of two input files

generate_mask.py	Generate mask file from input file
geocode.py	Resample radar-coded files into geo coordinates, or vice versa.
ifgram_inversion.py	Invert network of interferograms into time-series.
image_reconstruction.py	Reconstruct network of interferograms from time-series
image_math.py	Basic mathematic operation of input file(s)
info.py	Display metadata / structure of input file
load_data.py	Load a stack of interferograms into HDF5 files
load_gbis.py	Load the inversion result from GBIS software
load_hdf5.py	Load the binary file(s) into an HDF5 file
local_oscillator_drift.py	Correct local oscillator drift for Envisat data
mask.py	Mask input data file with input mask file by setting values on the unselected pixels into Nan or zero.
match.py	Merge two or more geocoded files which share common area into one file.
modify_network.py	Modify the network setting of an ifgramStack HDF5 file.
multilook.py	Multilook input file.
plot_coherence_matrix.py	Plot the coherence matrix of one pixel, interactively.
plot_network.py	Plot the network configuration of an ifgramStack file.
plot_transection.py	Plot the value of 2D matrix along a profile.
prep_aria.py	Prepare input data from ARIA GNUW products
prep_gamma.py	Prepare metadata file for GAMMA files.
prep_giant.py	Prepare metadata file for GIAnT files.

prep_isce.py	Prepare metadata file for ISCE files.
prep_roipac.py	Prepare metadata file for ROI_PAC files.
prep_snap.py	Prepare metadata file for SNAP geocoded products.
reference_date.py	Change the reference date of a time-series HDF5 file.
reference_point.py	Change the reference pixel of an input file.
remove_ramp.h5	Remove phase ramps for input file.
save_gbis.py	Save input files in GBIS *.mat file format.
save_gmt.py	Save input file in GMT *.grd file format.
save_hdfeos5.py	Save input time-series into HDF-EOS5 format.
save_kmz.py	Save input file into Google Earth raster image.
save_kmz_timeseries.h5	Save input file into Google Earth points, interactively.
save_roipac.py	Save input file into ROI_PAC style binary file format.
select_network.py	Select interferometric pairs from input baseline file.
smallbaselineApp.py	Routine time series analysis for small baseline InSAR stack.
spatial_average.py	Calculate average in space domain.
spatial_filter.py	Spatial filtering of input file.
subset.py	Generate a subset of (crop) input file.
temporal_average.py	Calculate average in time domain.
temporal_derivative.py	Calculate the temporal derivative of displacement time-series.
temporal_filter.py	Smooth time-series in time domain with a moving Gaussian window

`timeseries2velocity.py`	Invert time-series for the average velocity.
`timeseries_rms.py`	Calculate the root mean square for each acquisition of the input time-series file.
`tropo_phase_elevation.py`	Correct stratified tropospheric delay based on the empirical phase/elevation ratio method.
`tropo_pyaps.py`	Correct tropospheric delay estimated from global atmospheric model (GAM) using PyAPS software (Jolivet et al., 2011; 2014).
`tsview.py`	Interactive time-series viewer.
`unwrap_error_bridging.py`	Correct phase-unwrapping errors with bridging method.
`unwrap_error_phase_closure.py`	Correct phase-unwrapping errors with the phase closure method.
`view.py`	2D matrix viewer.

S4.2 Filters tools in space and time domain

The software supports filters in space or time domain built on skimage (van der Walt et al., 2014). Although filtering is not applied in the routine workflow, it is a useful tool to examine the deformation signal because it allows removing undesired signals. Fig. S15 shows an example, where we use spatial Gaussian filtering to confirm a patchy, rapid subsidence signal.

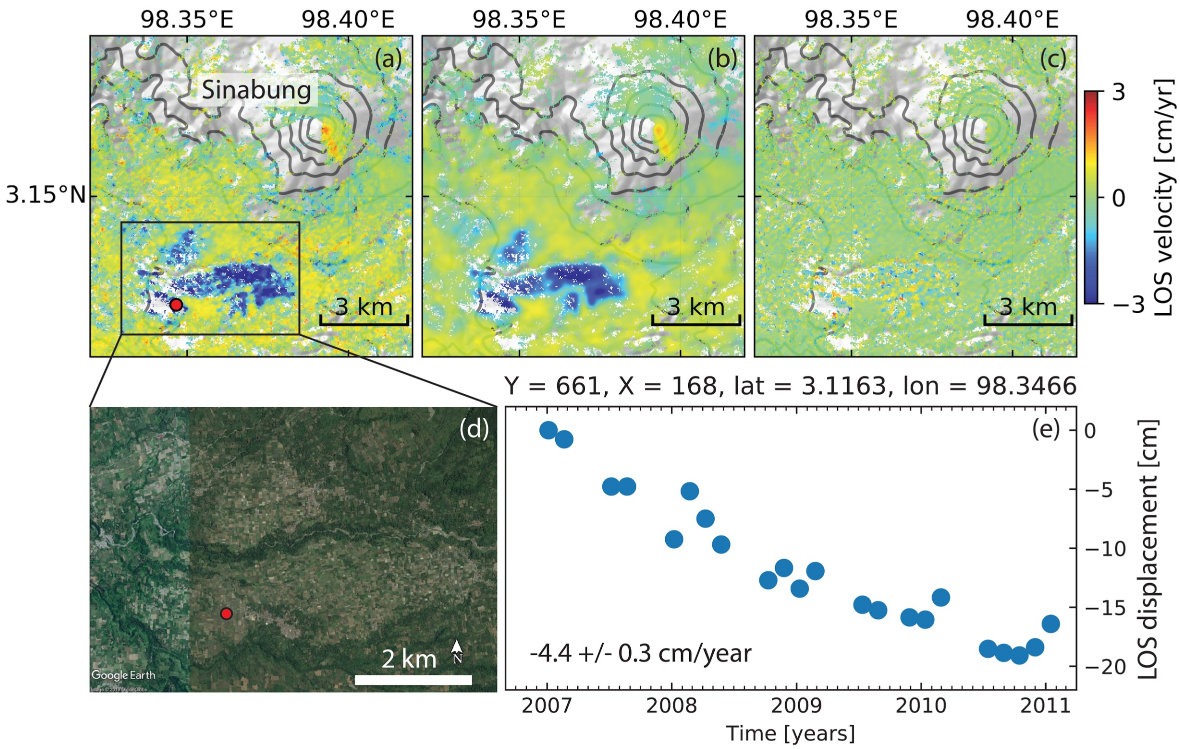

Figure S15. *Illustration of the spatial filtering. The LOS velocity from ALOS-1 ascending track 495 acquired over Sinabung volcano, Indonesia during January 2007 to January 2011 is used. (a) Original velocity in LOS direction, (b and c) velocities after lowpass and highpass Gaussian filtering with the standard deviation of 3.0. (a) is the sum of (b) and (c). The lowpass filtering eliminated the very short spatial wavelength features, thus, highlighted the relatively long spatial wavelength deformation features, such as the volcanic deformation along the Sinabung's southeast flank and an undocumented patchy, rapid subsidence area (up to -5.6 cm/year) is found ~6 km to the southwest of the volcano. The spatial pattern of the subsidence signal correlates well with the agricultural land use, suggesting that subsidence is caused by groundwater extraction (Chaussard et al., 2013). Reference point is a pixel at [E98.4999°, N3.1069°] outside of this figure. (d) Google Earth image for the marked rectangle area. (e) LOS displacement time-series for pixel marked by red circle in (a) at [E98.3466°, N3.1163°].*

S4.3 Interferometric pairs selection

The software supports several interferometric pairs selection methods to facilitate the pre-processing, such as small baseline, sequential, hierarchical, Delaunay triangulation, minimum spanning tree and star/PS-like methods, as shown in Fig. S16.

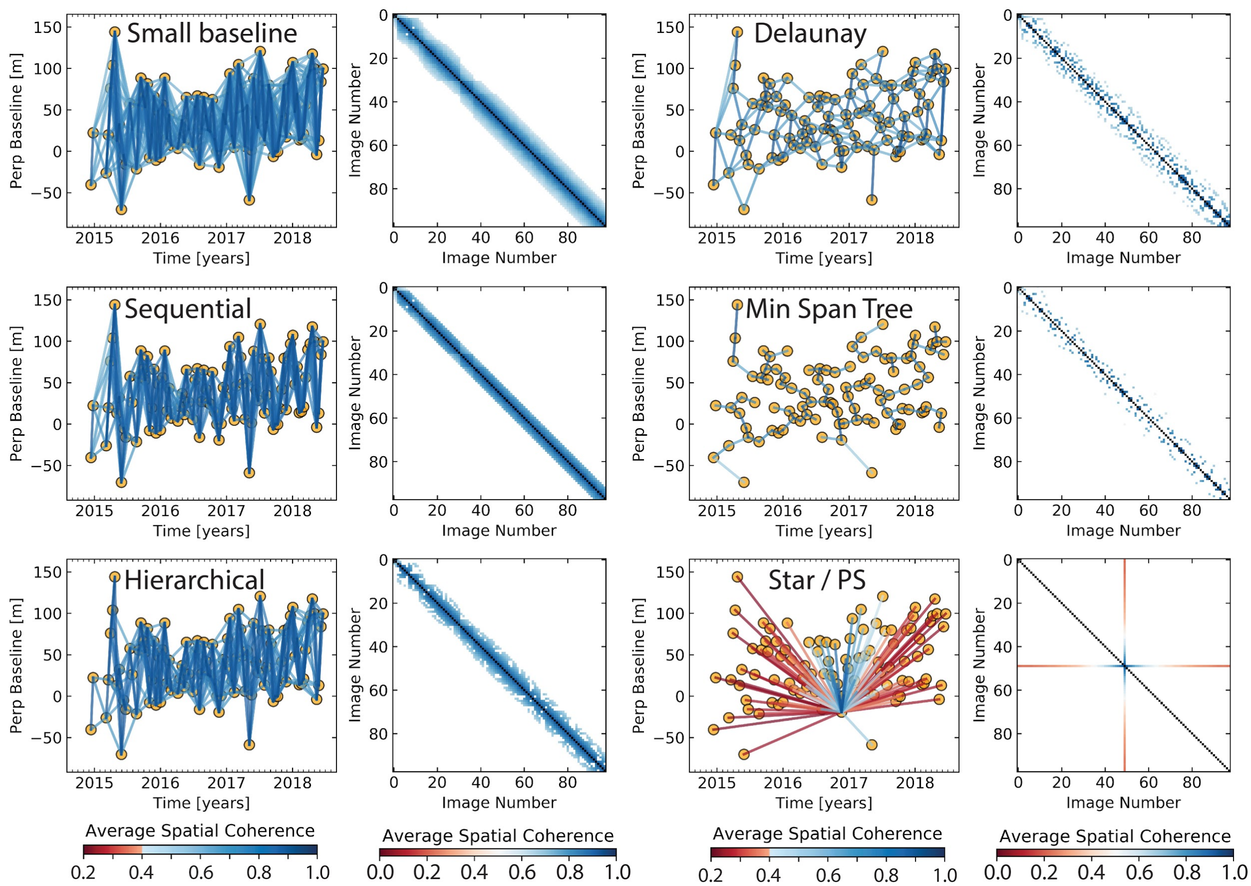

Figure S16. *Illustration of interferometric pairs selection. The temporal and perpendicular baselines are from Sentinel-1 dataset of section 5. For each method, network configuration on the left and the corresponding coherence matrix on the right. The spatial coherence calculation is described in section S3.1 with decorrelation rate of 200 days and long-term coherence of 0.2. The small baseline method selects interferograms with temporal and perpendicular baseline within the predefined thresholds (120 days and 200 m; Berardino et al., 2002). The sequential method selects for each acquisition with a predefined number (5) of its nearest neighbors back in* *time (Reeves and Zhao, 1999). The hierarchical method specifies a predefined list of temporal and perpendicular baselines as [6 days, 300 m; 12 days, 200 m; 48 days, 100 m; 96 days, 50 m], each pair of temporal and perpendicular thresholds selects interferograms the same as small baseline method (Zhao, 2017). The Delaunay triangulation method generates triangulations in the temporal and perpendicular baseline domain and selects interferograms within the predefined maximum temporal and perpendicular baseline (120 days and 200 m; Pepe and Lanari, 2006). The minimum spanning tree method calculates a spatial coherence value based on its simple relationship with the temporal and perpendicular baseline and selects N-1 interferograms that maximizes the total coherence (Perissin and Wang, 2012). The star-like method selects network of N-1 interferograms with single common reference acquisition (usually in the center of the time period; Ferretti et al., 2001).*

S4.4 Local oscillator drift correction for Envisat

Data from Envisat's Advanced Synthetic Aperture Radar instrument include a phase ramp in range direction due to timing errors. We correct this local oscillator drift using the empirical model given by Marinkovic and Larsen (2013).

$$\phi_{LOD}^{i} = \frac{-4\pi}{\lambda} 3.87 \times 10^{-7} r(t_i - t_1) \tag{S16}$$

where $(t_i - t_1)$ represents the time difference in years between SAR acquisition t_i and t_1 (see also Fattahi and Amelung, 2014). Since this model is independent of the InSAR phase measurement, this correction should be applied before any InSAR data-dependent phase corrections.

Supplemental references

Chaussard, E., F. Amelung, H. Abidin, and S.-H. Hong (2013), Sinking cities in Indonesia: ALOS PALSAR detects rapid subsidence due to groundwater and gas extraction, *Remote Sensing of Environment*, 128(0), 150-161, doi:10.1016/j.rse.2012.10.015.

Du, Y., L. Zhang, G. Feng, Z. Lu, and Q. Sun (2017), On the Accuracy of Topographic Residuals Retrieved by MTInSAR, *IEEE Transactions on Geoscience and Remote Sensing, 55*(2), 1053-1065, doi:10.1109/TGRS.2016.2618942.

Marinkovic, P., and Y. Larsen (2013), Consequences of long-term ASAR local oscillator frequency decay - An empirical study of 10 years of data, paper presented at *Proceedings of the Living Planet Symposium (abstract)*, European Space Agency, Edinburgh, U. K.

Reeves, S. J., and Z. Zhao (1999), Sequential algorithms for observation selection, *IEEE Transactions on Signal Processing*, *47*(1), 123-132, doi:10.1109/78.738245.

van der Walt, S., J. L. Schönberger, J. Nunez-Iglesias, F. Boulogne, J. D. Warner, N. Yager, E. Gouillart, and T. Yu (2014), scikit-image: image processing in Python, *PeerJ*, *2*, e453, doi:10.7717/peerj.453.

Zhao, W. (2017), Small Deformation Detected from InSAR Time-Series and Their Applications in Geophysics, Dissertation thesis, 153 pp, University of Miami, Miami, FL.